Solar Hydrogen Production: Techno-Economic Analysis of a Parabolic Dish-Supported High-Temperature Electrolysis System

Luca Mastropasqua[*,a], Ilaria Pecenati[b], Andrea Giostri[b], Stefano Campanari[b]

[a]Advanced Power and Energy Program, University of California, Irvine, CA 92697, USA

[b]Group of Energy Conversion Systems, Politecnico di Milano, Via Lambruschini 4, 20156 Milan – Italy

ABSTRACT

The roadmap for the hydrogen uptake passes through the development of near-zero emission and/or renewable technologies for hydrogen production. This is the rationale for the investigation of renewable power-to-fuel, namely the coupling between high temperature electrolysis and concentrating solar power. The proposed plant is conceived to supply hydrogen for a small refuelling station. It is based on solid oxide electrolyser cell technology, which performs water electrochemical reduction, in order to produce a target of 150 kg d^{-1} of hydrogen. The plant is integrated with a parabolic dish solar field designed to provide both electricity and thermal energy, necessary for the electrolysis reaction to take place. Specifically, a modular multi-dish configuration is selected, in which electric power is produced by 30 kW_{el} solarized micro-gas turbines placed in the dishes' focus. In addition to considering a pure renewable power input, a hybridization with natural gas is considered to face the variability of solar resource. Once a yearly H_2 yield is estimated, a preliminary

---

[*] Corresponding author: Luca Mastropasqua lm1@apep.uci.edu

economic analysis is carried out and the levelised cost of hydrogen is subsequently obtained. It is found that the system can be operated at a nominal solar-to-hydrogen efficiency above 30%, with a solid oxide electrolysis cell efficiency around 80%. In hybrid conditions, 10 parabolic dishes (9 generating electricity through the micro-gas turbines, 1 supplying heat to the solid oxide electrolysis cell) are needed to produce the target 150 kg d^{-1} of hydrogen. In conclusion, the competitiveness of the plant is evaluated in comparison with other solar fuels technologies.

KEYWORDS

Solid Oxide Electrolysis Cell; Concentrated Solar Power; Solar Hydrogen; Parabolic dish; Micro Gas Turbine; System analysis

INTRODUCTION

The global energy system is going towards the decarbonisation across the power, mobility and industrial sectors. In this energy transition, hydrogen plays a key role as it constitutes a clean and flexible energy carrier. Hydrogen could indeed be involved in power-to-gas applications, for direct injection into an existing natural gas infrastructure [1], and could be used as fuel for fuel cell vehicles in power-to-fuel applications. Moreover, it could serve as energy storage system, enabling a larger share of renewable energy to be integrated into the electric grid [2]. Hence, hydrogen can link different energy sectors and energy transportation and distribution networks and increase the operational flexibility of future low-carbon energy systems [3]. The roadmap for the hydrogen uptake passes through the development of near-zero emission technologies for hydrogen generation. In this respect, research on the coupling between a water splitting technology and a solar energy system has been taking root, leading to the so-called solar hydrogen production.

In the open literature, the modelling of Solid Oxide Electrolysis Cells (SOEC) is extensively studied. Thanks to the reversible feature of the cell, which can be employed either in fuel cell or electrolysis mode, previous experience on Solid Oxide Fuel Cells (SOFC) modelling can be conveniently exploited.

Udagawa et al., 2007 [4] develop a one-dimensional dynamic model of a cathode-supported planar SOECs. This is then employed to study the steady state behaviour of a SOEC stack at different current densities and temperatures. Menon et al., 2014 [5] propose a quasi-two-dimensional model in which the species composition is resolved in 1D in the gas channels (along the direction of axial flow) as well as in the porous media (transverse to the direction of axial flow). The simulation applies detailed models for electrochemical conversion at the three-phase boundary, an elementary heterogeneous reaction mechanism for the thermo-catalytic H_2 electrode chemistry, dusty-gas model to account for multicomponent diffusion through porous media, and a plug flow model for flow through the channels. Also the performance of SOEC in co-electrolysis mode, for syngas production, is studied in Menon et al., 2015 [6]. Ferrero et al., 2015 [7] develop a dynamic model for the simulation of planar reversible Solid Oxide Cells (rSOCs). In the study, the performance of commercial-size cells is investigated and an integrated thermo-electrochemical model is calibrated and validated on experimental data. AlZahrani et al., 2018 [8] performed a modelling optimization of a 1 MW_e SOEC system and evaluated energy and exergy efficiencies, respectively resulting in 85.15% and 83.41%. Xing et al., 2018 [9] propose a comprehensive energy flow model to optimise the operation of a SOEC system at various loading conditions. Other works devoted to rSOC modelling are also available (Kazempoor and Braun [10,11], Wendel et al., 2015 [12], Ni et al., [13] and Wang et al., [14]).

Among the solar hydrogen technologies, attention is drawn to the coupling between SOEC and a Concentrated Solar Power (CSP) system. The reason is that CSP offers the opportunity to deliver both electricity and high temperature heat at the same site, so it can fulfil the energy requirements of the SOEC, in terms of electric and thermal duty. As a result, the combination of hydrogen production by high temperature electrolysis and concentrated solar energy is very attractive since it could create synergies with gains for both technologies. A variety of solar hydrogen solutions have been developed with different operating conditions and applications. Derbal-Mokrane et al., [15] propose a system that integrates high temperature electrolysis with a parabolic trough section, devoted to thermal energy production. The electric input is provided separately by a PV power station. Results show that the power requirement for a hydrogen throughput of 400 kg h^{-1} is of 5 MW_{th} thermal and 14 MW_{el} electric power; about 140,000 m^2 area is necessary, of which more than 90% is for the PV field.

Also Seitz et al., [16] suggest the integration of a SOEC and a parabolic trough system at a MW-scale. They studied the effect of a phase-change material storage (PCM) for the extension of hydrogen production during no-sun hours. They concluded that with a Thermal Energy Storage (TES) capacity of 25.6 MWh, the production time can increase by 50%, which translates to a reduction by 34% in the Levelised Cost Of Hydrogen (LCOH). Mohammadi and Mehrpooya [17] adopt the same CSP technology, though designed to provide both thermal and electric energy required for the electrolysis process, with the purpose of increasing the system efficiency and reducing the total land occupation. Part of the thermal energy from solar trough collectors is delivered to an ORC (Organic Rankine Cycle) for electricity production; a TES is also included to ensure continuous operation. . Sanz-Bermejo et al., [18] study the coupling of SOEC with a 10 MW_e direct steam generation solar tower plant. The solar system is designed to cover the electric consumption of the SOEC stack, of the overall balance of plant, as well as the heat demand of the electrolyser. The results show that when the stack is operated at atmospheric pressure, the efficiency losses of the solar plant can be reduced by 60% if process steam is extracted from low pressure turbine section and solar plant feed water is preheated with rejected hot streams from the electrolyser. In pressurized mode, the reference hybrid plant efficiency improves by 5.8% and, if PSA (Pressure Swing Adsorption) is included, oxygen is obtained as co-product. In another publication of Sanz-Bermejo et al., [19], a power-to-gas plant is presented, in which a grid-connected SOEC is combined with a Linear Fresnel technology, and a ceramic TES. The collectors oversee the evaporation of the reacting feed water, while electrical heaters supply the thermal power to achieve the electrolyser's operating temperature (700°C). The nominal target of 400 kg d^{-1} of hydrogen is accomplished and, depending on the number of TES modules, it can reach values above 550 kg d^{-1}. In addition, it is considered a scenario in which the SOEC can operate reversibly for grid balancing.

The feasibility of a solar tower system coupled with SOEC is analysed by Lin and Haussener [20], providing evidence that, among different proposed scenarios, this solution is able to work at a remarkable solar-to-hydrogen efficiency (10.6%), but at the expense of a greater LCOH ($8.19/kg).

To the best knowledge of the authors, only one work has explored a techno-economic analysis of a coupling between SOEC and a parabolic dish solar system for producing around 41 kg d^{-1} of hydrogen. Mohammadi et al., 2018 [21] propose a 0-dimensional model of a compressed air storage system coupled with a solar dish collector to supply electric power to a high temperature electrolyser, whilst another dish collector supplies thermal power to the cathode side of the SOEC stack. Moreover, in case the dish collector is not able to supply all the thermal power required by the stack, an electric heater is used as a complementary heat source.

In this work, on the other hand, the analysis is expanded by studying a SOEC system design at both atmospheric and pressurised operation and its thermal integration with the solar system with or without sweep gas. The SOEC operation is described via the development of a new 1-dimensional model. Moreover, the techno-economic analysis proposed herein is focused on designing a system sized for a typical hydrogen refuelling station serving approximately 30 light duty vehicles per day.

The modular and distributed nature of the parabolic dish collector and the modularity of the high temperature electrolysis system allow a synergistic system integration, virtually without the need for an electric grid connection and the possibility of installation in remote areas. This work specifically aims at addressing the main challenges of high temperature electrolysis systems, namely the thermal integration with the heat source and the thermal management of the electrolyser stack.

Thermodynamics of High Temperature Electrolysis

Focus is made on High Temperature Electrolysis, notably on the solid oxide electrolysis cell technology. Thanks to the operation at temperatures above 650°C, SOEC systems can take advantage of reducing the required electric energy for the process itself. In fact, when an electrolytic cell operates at constant temperature and pressure, the required energy for water electrolysis reaction is determined by the process enthalpy change (ΔH). For this reaction to take place, part of the energy is supplied by electric energy (W), and this part corresponds to the Gibbs free energy change (ΔG). The rest is supplied by thermal energy (Q) and equals the product of the process temperature (T) and the entropy change (ΔS) [22]. The relation among these thermodynamic quantities is:

$$\Delta G = \Delta H - Q = \Delta H - T\Delta S \qquad \textit{Eq. 1}$$

The minimum reversible voltage or equilibrium voltage required for water splitting at standard conditions (298 K and 101,325 Pa) is given by:

$$\mathrm{E_{rev}} = \frac{\Delta G^{0}_{298K}}{2 \times \mathcal{F}} = \frac{237{,}200\, J/mol}{2 \times 96485} = 1.23\ \mathrm{V} \qquad \textit{Eq. 2}$$

where two Faraday units ($\mathcal{F}$ is the Faraday's constant, equal to 96,485 C mol^{-1}) correspond to nearly 53.6 Ah and allow to generate 1 mol of hydrogen. However, water splitting is an endothermic reaction, requiring also heat to be carried out at constant temperature. If the thermal energy $T\Delta S$ required is fully provided by cell internal losses (e.g. Joule losses and other polarization losses) – hence no thermal energy addition is performed – the actual minimum voltage for the dissociation increases above $\mathrm{E_{rev}}$ and it is defined as the thermoneutral voltage V_{tn}, obtained from the following expression:

$$V_{tn} = \frac{\Delta H}{2\mathcal{F}} \qquad \textit{Eq. 3}$$

Heat sinks and sources are linked to two phenomena: i) electrochemical reaction, which is endothermic; ii) polarization loss mechanisms, which release heat. The water splitting or steam reduction reaction is endothermic, therefore thermal energy is consumed by the electrolysis reaction. The reaction heat flux Q_{react} $[W\ m^{-2}]$ is derived as follows:

$$Q_{react} = \frac{j}{2\mathcal{F}} T\Delta S = \frac{j}{2\mathcal{F}}(\Delta H - \Delta G) = j(V_{tn} - E_N) \qquad \textit{Eq. 4}$$

Where j is the current density, E_N is the Nernst voltage or ideal cell voltage (defined starting from the standard $\mathrm{E_{rev}}$ and depending on temperature, pressure and reactant concentrations, see also Eq. 9 in the following) and ΔS is the entropy change of the electrolysis reaction, which is dependent on the reactants and products partial pressures and the operating temperature.

The polarization heat flux Q_{loss} $[W\ m^{-2}]$ is the heat generated by overpotentials, in particular by Joule effect and by other non-ohmic irreversibilities. It is given by:

$$Q_{loss} = j(V - E_N) = j(\sum \Delta V_{losses}) \qquad \text{Eq. 5}$$

The net thermal flux is the difference between the abovementioned quantities:

$$Q_{SOEC} = Q_{react} - Q_{loss} = j(V_{tn} - V) \qquad \text{Eq. 6}$$

This means that, depending on the operating voltage, the net heat generation in the SOEC may be negative, zero, or positive. This phenomenon is depicted in Figure 1. The figure shows the respective internal heat sink/source fluxes associated with the electrochemical reaction and the ohmic heating.

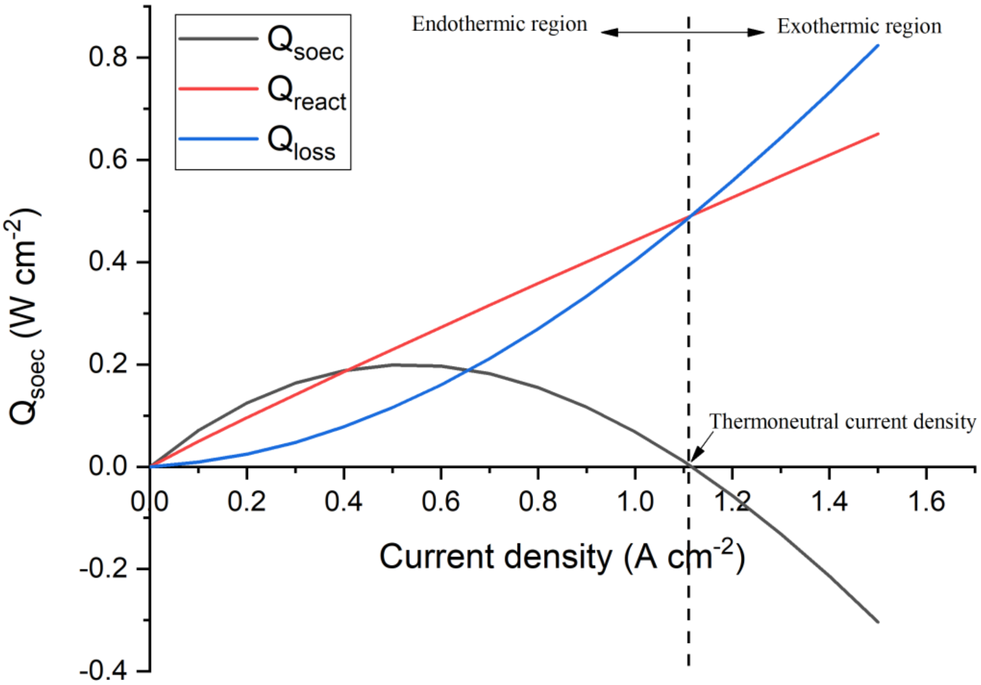

Figure 1 - Variation with current density of Q_{react} and Q_{loss} and resulting Q_{SOEC} at 800°C ($\Delta H = 248.3$ kJ mol^{-1}, $\Delta G = 188.5$ kJ mol^{-1}, $\Delta S = 0.05575$ kJ mol^{-1}K^{-1})

Consider the isothermal operation of the SOEC cell. These are the possible conditions that can arise:

- $V < E_N$: no water electrolysis can occur.
- $E_N < V < V_{tn},\ Q_{SOEC} > 0$: electrolysis is possible by addition of heat (endothermic conditions) in order to maintain isothermal operation.
- $V = V_{tn},\ Q_{SOEC} = 0$: the cell is adiabatic, therefore that heat provided by irreversible losses is enough to sustain the endothermic electrolysis reaction; the entire enthalpy change in the electrolysis is exactly matched by the electrical energy input to the cell.
- $V > V_{tn}, Q_{SOEC} < 0$: electrolysis takes place under heat dissipation (exothermic conditions) to keep isothermal operation. The power supplied to the cell is greater than the minimum required by the process ($V_{tn} \cdot j$). The cell consumes an extra power $\dot{Q}_{SOEC}$ due to cell losses; the temperature of the process rises unless the cooling system evacuates the excess heat [22].

In summary, the thermoneutral voltage separates the endothermic behaviour of the SOEC (below V_{tn}) from the exothermic one (above V_{tn}). The same happens in terms of current density, as shown in Fig. 1. Note that the share of heat input supplied by internal irreversibilities increases with higher current density; however, this brings about a higher voltage and a higher electric consumption (or in other terms, a lower electric efficiency) The SOEC electric efficiency is indeed defined as:

$$\eta_{el} = \frac{\dot{m}_{H2} \times LHV}{\dot{W}_{el}} = \frac{\dot{m}_{H2} \times LHV}{jA \times V} \qquad \textit{Eq. 7}$$

On the other hand, when operating at lower current density, a larger stack area is needed (i.e., lower power density, $W\ m^{-2}$) to support a given hydrogen production rate, leading to a higher system capital cost [4]. Due to this trade-off, a techno-economic analysis should be performed to optimize the SOEC functioning.

Given this background, this work focuses on small scale hydrogen production system, specifically conceived for the hydrogen distribution network. Hydrogen refuelling stations could be directly supplied on site, leading to the minimization of the transmission and distribution costs [23].

Therefore, this study proposes the design of a novel solar driven hydrogen production plant, by coupling a SOEC to a parabolic dish solar system. From a design perspective, a multi-dish configuration is selected, in which the share of electric power is produced by an open-cycle air Micro Gas Turbine (MGT) placed in the dish focus. The required thermal power is produced by means of a dedicated thermal receiver which brings the anodic and cathodic streams to the cell operating temperature. To gain insight into the operation of the SOEC within the plant, a 1D cell model is studied, enabling a detailed description of the cell from the electrochemical and thermodynamic standpoint. A techno-economic optimization is subsequently performed to assess the optimal design conditions of the plant. Finally, the competitiveness of the plant is evaluated in comparison with other solar hydrogen production technologies.

METHODOLOGY

SOEC modelling

A new one-dimensional SOEC model is built using Aspen Custom Modeler (ACM) with aim of reproducing a planar co-flow flow-field configuration. The cell is discretised axially in a number of finite volumes and for each of them the electrochemical, mass and energy balances are solved. The following assumptions are used in the development of the model:

- Iso-potential electrodes along the cell axial length;
- lumped electrodes-electrolyte assembly temperature at each unit element;

- equivalent cell channels from both thermodynamic and fluid-dynamic perspective;
- negligible pressure gradient across the fuel and sweep channels;

Fuel (fu) electrode and sweep (sw) electrode designations are used here instead of cathode and anode. The electrochemical semi-reaction of hydrogen oxidation and oxygen reduction are reported hereafter:

$$H_2 + O^{2-} \leftrightarrow H_2O + ze^- \quad \text{Eq. 8}$$

$$O_2 + 2ze^- \leftrightarrow 2O^{2-} \quad \text{Eq. 9}$$

where, the number of charge carriers transferred z is equal to 2 for the hydrogen electro-oxidation and $2z$ for the oxygen electro-reduction reaction. In this work, we assume that negative currents are specified for electrolysis and positive currents indicate operation in fuel cell mode.

Electrochemical model

The cell voltage is computed as:

$$V_{cell} = E_N - \eta_{ohm} - \eta_{act} - \eta_{conc} \quad \text{Eq. 10}$$

where, η_{ohm}, η_{act} and η_{conc} are respectively the ohmic, activation and concentration overpotentials, responsible for the deviation of the cell voltage from the Nernst potential $\mathrm{E_N}$, expressed by the Nernst's law:

$$E_N = -\frac{\Delta G}{2\mathcal{F}} + \frac{\mathcal{R}T_{PEN}}{2\mathcal{F}} ln \frac{x_{H_2} x_{O_2}^{\frac{1}{2}}}{x_{H_2O}} + \frac{\mathcal{R}T_{PEN}}{4\mathcal{F}} ln \left(\frac{p_{sw}}{p_0}\right) \qquad \text{Eq. 11}$$

where the Nernst potential is evaluated at the electrodes-electrolyte assembly (Positive-Electrode-Negative – PEN – structure) temperature, the species molar fractions (x_{H_2}, x_{O_2} and x_{H_2O}) are those in the gas bulk and p_0 is the reference pressure (i.e., 1 atm).

The Ohm's law is used to describe ohmic losses:

$$\eta_{ohm} = R_{eq,tot} j \qquad \text{Eq. 12}$$

$$R_{eq,tot} = R_{sw} + R_{fu} + R_{el} + R_c \qquad \text{Eq. 13}$$

where, the resistances related to the PEN structure are calculated as the ratio of the thickness to the conductivity of the considered layer. R_{sw}, R_{fu} and R_{el} are respectively the ohmic resistances of the sweep and fuel electrodes and of the electrolyte; whilst, R_c accounts for possible contact resistances at the electrode-electrolyte or electrode-interconnect interphases. A summary of the electric conductivities of the materials considered is reported in Table 1.

Table 1 - Model input values used for validation. Data from [5,24]

Cell geometry	**Description**	**Value**
δ_{fu} / μm	Fuel electrode thickness	310
δ_{sw} / μm	Sweep electrode thickness	10
δ_{el} / μm	Electrolyte thickness	10
L / m	Channel length	0.01852

W / m	Channel width	0.00926
H_{fu} / m	Fuel electrode height	0.001
H_{sw} / m	Sweep electrode height	0.001
Material electrical properties		
σ_{fu} / $S\ m^{-1}$	Fuel electrode electronic conductivity	$\frac{10^7}{T_{PEN}}\exp\left(\frac{1150}{T_{PEN}}\right)$
σ_{sw} / $S\ m^{-1}$	Sweep electrode electronic conductivity	$\frac{4.6\cdot 10^6}{T_{PEN}}\exp\left(\frac{1100}{T_{PEN}}\right)$
σ_{el} / $S\ m^{-1}$	Electrolyte ionic conductivity	$\frac{3.6\cdot 10^7}{T_{PEN}}\exp\left(\frac{-8\cdot 10^4}{\mathcal{R}T_{PEN}}\right)$
Electro-kinetic parameters		
E_{act}^{fu} / $kJ\ mol^{-1}$ (fitted)	Fuel electrode activation energy	87.4
E_{act}^{sw} / $kJ\ mol^{-1}$ (fitted)	Sweep electrode activation energy	88.75
γ_{fu} / $A\ m^{-2}$	Fuel electrode pre-exponential factor	3.504 10^8
γ_{sw} / $A\ m^{-2}$	Sweep electrode pre-exponential factor	1.698 10^8
β_{fu} / -	Fuel electrode symmetry factor	0.5

β_{sw} / -	Sweep electrode symmetry factor	0.5
Electrodes microstructure		
ϕ / -	Porosity	0.35
τ / -	Tortuosity	3.0
r_{pore} / μm	Average pore radius	0.15
Energy balance-related properties		
ρ_{PEN} / $kg\ m^{-3}$	PEN density	5900
ρ_{int} / $kg\ m^{-3}$	Interconnect density	8000
$c_{p,PEN}$ / $kJ\ kg^{-1}\ K^{-1}$	PEN heat capacity	0.5
$c_{p,int}$ / $kJ\ kg^{-1}\ K^{-1}$	Interconnect heat capacity	0.5
k_{PEN} / $W\ m^{-1}\ K^{-1}$	PEN thermal conductivity	2.0
k_{int} / $W\ m^{-1}\ K^{-1}$	Interconnect thermal conductivity	25.0
ϵ_{PEN} / -	PEN emissivity	0.8
ϵ_{int} / -	Interconnect emissivity	0.1

The total activation overpotential includes contributions from both the fuel and sweep electrodes; the model presented by Zhu et al., 2005 [25] is implemented. The modified Butler-

Volmer equation, which describes the functional relationship between the activation losses and current density, is:

$$j = j_{0,fu}\left[exp\left(\frac{(\beta_{a,fu}+1)\mathcal{F}\eta_{act,fu}}{\mathcal{R}T_{PEN}}\right) - exp\left(-\frac{\beta_{a,fu}\mathcal{F}\eta_{act,fu}}{\mathcal{R}T_{PEN}}\right)\right] \qquad \textit{Eq. 14}$$

$$j = j_{0,sw}\left[exp\left(\frac{(\beta_{a,sw}+1)\mathcal{F}\eta_{act,sw}}{\mathcal{R}T_{PEN}}\right) - exp\left(-\frac{\beta_{a,sw}\mathcal{F}\eta_{act,sw}}{\mathcal{R}T_{PEN}}\right)\right] \qquad \textit{Eq. 15}$$

where, $j_{0,fu}$ and $j_{0,sw}$ are the exchange current densities, expressed as

$$j_{0,fu} = j^{*}_{H_2}\frac{\left(\frac{p_{H_2}}{p^{*}_{H_2}}\right)^{\frac{\beta_{a,fu}}{2}}\left(\frac{p_{H_2O}}{p_0}\right)^{1-\frac{\beta_{a,fu}}{2}}}{1+\left(\frac{p_{H_2}}{p^{*}_{H_2}}\right)^{\frac{1}{2}}} \qquad \textit{Eq. 16}$$

$$j_{0,sw} = j^{*}_{O_2}\frac{\left(\frac{p_{O_2}}{p^{*}_{O_2}}\right)^{\frac{\beta_{a,sw}}{2}}}{1+\left(\frac{p_{O_2}}{p^{*}_{O_2}}\right)^{\frac{1}{2}}} \qquad \textit{Eq. 17}$$

where, the equilibrium pressures $p^{*}_{H_2}$ and $p^{*}_{O_2}$ for common electrode materials (e.g., a Ni-YSZ/YSZ and LSM/YSZ interphase) are respectively [10,25]:

$$p^{*}_{H_2} = 2.1362\cdot 10^{5}\, exp\left(-\frac{9.6\cdot 10^{4}}{\mathcal{R}T_{PEN}}\right)\ [atm] \qquad \textit{Eq. 18}$$

$$p^{*}_{O_2} = 4.9\cdot 10^{8}\, exp\left(-\frac{200\cdot 10^{3}}{\mathcal{R}T_{PEN}}\right)\ [atm] \qquad \textit{Eq. 19}$$

The following Arrhenius expressions are employed for describing $j^{*}_{H_2}$ and $j^{*}_{O_2}$:

$$j^*_{H_2} = \gamma_{fu}\, exp\left(-\frac{E^{fu}_{act}}{\mathcal{R}T_{PEN}}\right) \qquad \text{Eq. 20}$$

$$j^*_{O_2} = \gamma_{sw}\, exp\left(-\frac{E^{sw}_{act}}{\mathcal{R}T_{PEN}}\right) \qquad \text{Eq. 21}$$

The total concentration overpotential is defined as the difference between the theoretical Nernst potential in Eq. 11, which is based on the bulk flow chemical composition, and the local Nernst potential, calculated with the molar fractions of the species at the Triple Phase Boundary (TPB). By rearranging, it is possible to identify two terms, related to the fuel and sweep sides

$$\eta_{conc,fu} = \left(\frac{\mathcal{R}T_{PEN}}{2\mathcal{F}}\right) ln\left(\frac{x_{H_2}x_{H_2O,TPB}}{x_{H_2,TPB}x_{H_2O}}\right) \qquad \text{Eq. 22}$$

$$\eta_{conc,sw} = \left(\frac{\mathcal{R}T_{PEN}}{4\mathcal{F}}\right) ln\left(\frac{x_{O_2}}{x_{O_2,TPB}}\right) \qquad \text{Eq. 23}$$

The computation of the species molar fraction at cell reaction sites is performed as done by [26]. The reactants species diffusive mass transport path involves the transport from the gas bulk flow composition $x_{i,b}$ to the electrode surface layer $x_{i,l}$ and then the diffusion through the cell porous electrode to cell reaction sites $x_{i,TPB}$. For products species, the path is in the opposite direction. Fick's law is implemented to derive the mole fraction at the surface electrode and at the TPB.

Fuel Electrode

$$x_{i,l} = x_{i,b} \mp \frac{\mathcal{R}T_{fu}j}{2\mathcal{F}p_{fu}D_{mix,i}}\frac{H_{fu}}{2}; i = H_2, H_2O \qquad \text{Eq. 24}$$

$$x_{i,TPB} = x_{i,l} \mp \frac{\mathcal{R}T_{PEN}j}{2\mathcal{F}p_{fu}D_i^{eff}}\delta_{fu} \qquad \text{Eq. 25}$$

Sweep Electrode

$$x_{O_2,l} = 1 + \left(x_{O_2,b} - 1\right) exp\left(\frac{\mathcal{R}T_{sw}j}{4\mathcal{F}p_{sw}D_{mix,i}}\frac{H_{sw}}{2}\right) \qquad \text{Eq. 26}$$

$$x_{O_2,TPB} = 1 + \left(x_{O_2,l} - 1\right) exp\left(\frac{\mathcal{R}T_{PEN}j}{4\mathcal{F}p_{sw}D_{O_2}^{eff}}\delta_{sw}\right) \qquad \text{Eq. 27}$$

In the channels, only molecular diffusion takes place. Binary diffusivities $D_{i,j}$ are calculated using Aspen procedures, given the species composition and the operating conditions (in terms of temperature and pressure of the anodic and cathodic streams). In case of a mixture of N species, the following mixing rule is applied to the molecular diffusion coefficients:

$$D_{mix,i} = \frac{1 - x_i}{\sum_{j\neq i}^{N}\frac{x_j}{D_{i,j}}} \qquad \text{Eq. 28}$$

Diffusion within the electrodes porous structure is modelled via a Knudsen diffusion term (Eq. 34). Molecular diffusion is dominant when the pore size is much larger than the mean free path of the molecular species; vice versa, the Knudsen diffusion becomes important when the pore size is much smaller than the mean free path of the molecular species. Therefore, the diffusion process between the electrode surface and the TPB will be governed by both molecule-molecule interaction and by molecule-pore wall interaction [13].

$$D_{Kn,i} = \frac{2}{3} r_{pore} \sqrt{\frac{8\mathcal{R}T_{PEN}}{\pi MM_i}} \qquad \text{Eq. 29}$$

Finally, an effective diffusivity is calculated, by combining the two diffusion mechanisms and by accounting for the tortuosity τ and porosity ϕ of the electrode microstructure.

$$\frac{1}{D_i^{eff}} = \frac{\tau}{\phi}\left(\frac{1}{D_{mix,i}} + \frac{1}{D_{Kn,i}}\right) \qquad \text{Eq. 30}$$

Mass and energy balances

Mass and energy balances are written and solved in each control volume along the cell axial length. The mass balance is solved for the two channels (i.e., fuel and sweep side) whilst the energy balance is divided into five sections: i) interconnect on fuel side; ii) fuel channel; iii) electrodes-electrolyte assembly structure; iv) sweep channel; v) interconnect on the sweep side.

Temperature inside each volume is considered uniform and the axial conduction in the solid structure is neglected for simplicity. As a result, five temperature layers are found. All the balances are written specific to the volume of the considered layer.

The mass and energy balances considered in this study are summarised hereafter:

Fuel Electrode

$$\frac{\partial C_i}{\partial t} = -\frac{\partial\left(u_{fu}C_i\right)}{\partial x} + \frac{\nu_i r_{red}}{H_{fu}} \qquad \text{Eq. 31}$$

$$\begin{aligned}\frac{\partial C_{fu}h_{fu}}{\partial t} = &-\frac{\partial(uCh)_{fu}}{\partial x} - \frac{j}{2\mathcal{F}H_{fu}}\left(h_{H_2} - h_{H_2O}\right) + \frac{k_{PEN,fu}}{H_{fu}}\left(T_{PEN} - T_{fu}\right) \\ &+ \frac{k_{PEN,fu}}{H_{fu}}\left(T_{int,fu} - T_{fu}\right)\end{aligned} \qquad \text{Eq. 32}$$

Sweep Electrode

$$\frac{\partial C_i}{\partial t} = -\frac{\partial (u_{sw} C_i)}{\partial x} + \frac{\nu_i r_{ox}}{H_{sw}} \qquad \textit{Eq. 33}$$

$$\frac{\partial C_{sw} h_{sw}}{\partial t} = -\frac{\partial (uCh)_{sw}}{\partial x} - \frac{j}{4\mathcal{F} H_{sw}} h_{O_2} + \frac{k_{PEN,sw}}{H_{sw}} (T_{PEN} - T_{sw}) + \frac{k_{PEN,sw}}{H_{sw}} \left(T_{int,sw} - T_{sw}\right) \qquad \textit{Eq. 34}$$

PEN Structure

$$\rho_{PEN} c_{p,PEN} \frac{\partial T_{PEN}}{\partial t} = k_{PEN} \frac{\partial^2 T_{PEN}}{\partial x^2} + \frac{j}{2\mathcal{F} \delta_{PEN}} \left(h_{H_2} - h_{H_2O}\right) + \frac{j}{4\mathcal{F} H_{sw}} h_{O_2} - \frac{jV}{\delta_{PEN}} + \frac{k_{PEN,fu}}{\delta_{PEN}} \left(T_{fu} - T_{PEN}\right) + \frac{k_{PEN,sw}}{\delta_{PEN}} (T_{sw} - T_{PEN}) - \frac{1}{\delta_{PEN}} \frac{\sigma\left(T_{PEN}^4 - T_{int,fu}^4\right)}{\frac{1}{\epsilon_{PEN}} + \frac{1}{\epsilon_{int}} - 1} - \frac{1}{\delta_{PEN}} \frac{\sigma\left(T_{PEN}^4 - T_{int,sw}^4\right)}{\frac{1}{\epsilon_{PEN}} + \frac{1}{\epsilon_{int}} - 1} \qquad \textit{Eq. 35}$$

Interconnectors

$$\rho_{int} c_{p,int} \frac{\partial T_{int,fu}}{\partial t} = k_{int} \frac{\partial^2 T_{int,fu}}{\partial x^2} + \frac{k_{PEN,fu}}{\delta_{int}} \left(T_{fu} - T_{int,fu}\right) + \frac{1}{\delta_{int}} \frac{\sigma\left(T_{PEN}^4 - T_{int,fu}^4\right)}{\frac{1}{\epsilon_{PEN}} + \frac{1}{\epsilon_{int}} - 1} \qquad \textit{Eq. 36}$$

$$\rho_{int} c_{p,int} \frac{\partial T_{int,sw}}{\partial t} = k_{int} \frac{\partial^2 T_{int,sw}}{\partial x^2} + \frac{k_{PEN,sw}}{\delta_{int}} \left(T_{sw} - T_{int,sw}\right) + \frac{1}{\delta_{int}} \frac{\sigma\left(T_{PEN}^4 - T_{int,sw}^4\right)}{\frac{1}{\epsilon_{PEN}} + \frac{1}{\epsilon_{int}} - 1} \qquad \textit{Eq. 37}$$

where, $k_{PEN,fu}$ is the convective heat transfer coefficient between the PEN structure and the fuel flow, and $k_{PEN,sw}$ between the PEN and the sweep flow. These parameters are assumed to be equivalent also for convective heat transfer over the interconnect structures; they are derived assuming constant Nusselt’s number and hydraulic diameter [4].

Despite the general formulation of the model is dynamic, we do not take into account in this work the effects of transient operation. Therefore, the derivatives vs. time in Eq. 31-Eq. 37 are all equal to zero in the following simulations.

The momentum balance is neglected in the model as it has been demonstrated to have a weak impact on the cell performance by Iora et al., [27]. They demonstrated that the cell efficiency differs by less than 1% and the gas outlet temperature difference is about 5 K compared to the same model with momentum balance. Hence the adoption of this hypothesis is considered to yield a sufficiently accurate prediction of the overall cell performance.

Plant modelling

The plant is conceived to supply hydrogen for a small refuelling station in Lancaster, California (34°41′N-118°9′W), for which the solar irradiation profile is available for one year with an hourly time step [28]. The location is set in order to provide a good siting of the solar plant in terms of annual mean solar direct irradiation (2989 kWh m^{-2} y^{-1}), whilst it is not considered at this time the strategic siting of the hydrogen station within a hydrogen distribution network. However, the solar irradiation can be considered representative also of nearby areas, not far from one of the many hydrogen stations which are currently under deployment in California. A hydrogen throughput of 150 kg d^{-1} is set as design capacity of the station (corresponding to nearly 30 cars refilling per day). Atmospheric as well as pressurised operation are evaluated.

Two plant layouts are proposed. Figure 2a and Figure 2b respectively depict the configuration of the SOEC module with and without sweep gas. The implementation of the plant model is performed using Aspen Plus®.

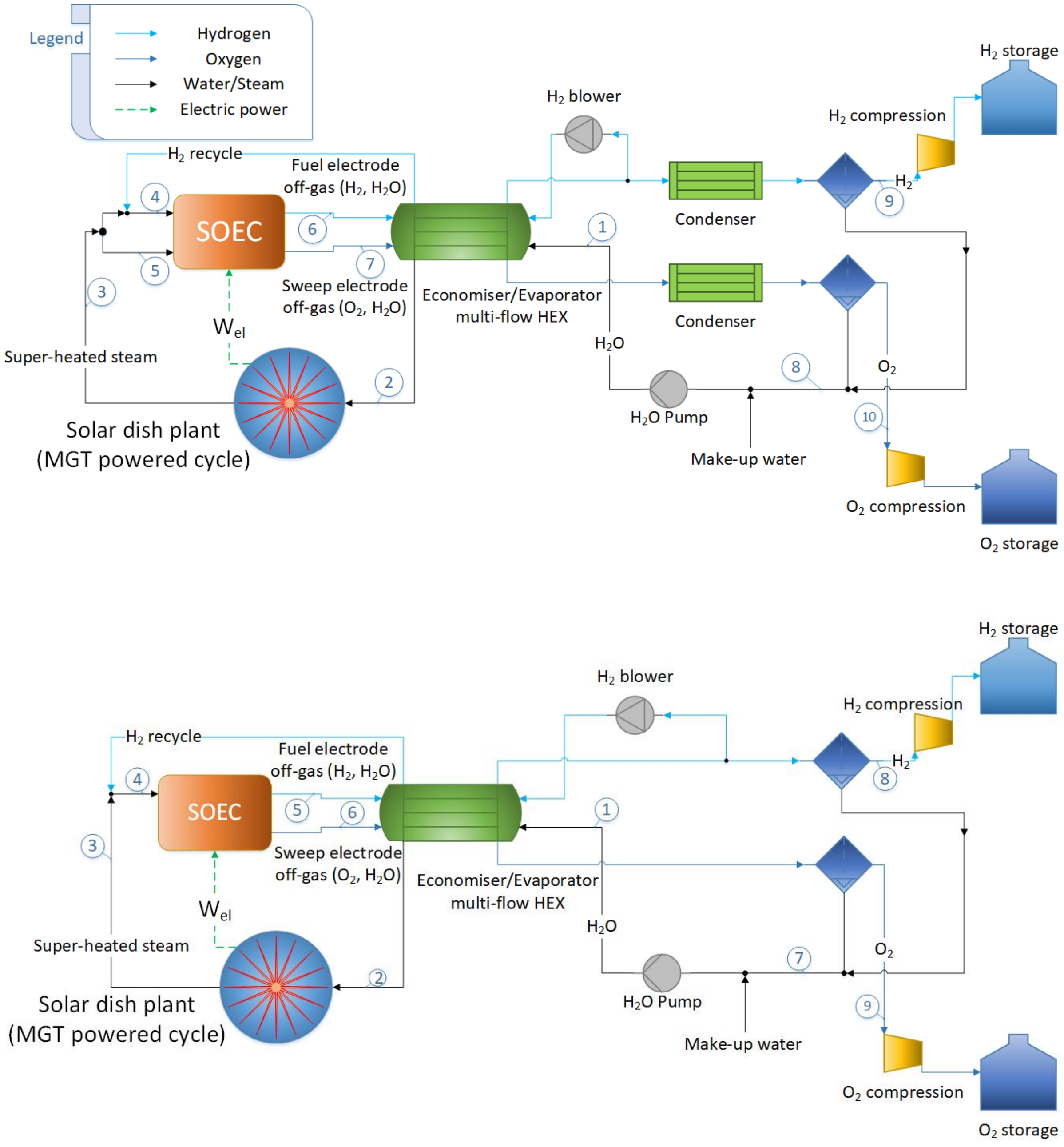

Figure 2 – Simplified schematic of the two plant configurations proposed: a) SOEC system with sweep gas on the sweep electrode; b) SOEC system without sweep gas on the sweep electrode;

In Figure 2a, the streams entering the electrode compartments of the SOEC stack are preheated to the design temperature (750°C) in a single stream (stream 3). The feed water (stream 1) passes first through a multiple flow heat exchange section (comprising of economiser and evaporator), then it is directed to the solar plant (simulated by a heater block), where superheated steam at 750°C is produced (stream 3) with a direct steam generation arrangement.

The sweep gas flow is set by controlling the split fraction downstream the solar dish. The leftover steam, with the addition of the hydrogen recycle, creates the fuel flow to the fuel electrode compartment (stream 4). The products of the electrolysis reaction are a mixture of H_2 and H_2O at the fuel electrode (stream 6), and steam enriched with O_2 at the sweep electrode side (stream 7). Both streams represent the hot streams in the heat exchange section. At the exit of the economiser, they are further cooled in two different condensers. The hydrogen recycle is separated before the condenser, re-compressed through a H_2 recirculation blower and re-heated before reinjection into the fuel electrode. Two adiabatic flashes allow for the condensate separation, which is then recycled to provide process water to the system (stream 8). On the other hand, the hydrogen (stream 9) and oxygen (stream 10) flows are sent each one to an intercooled compression unit and pressurised up to 200 bar for storage. A feed water pump, electrically driven, is needed to recover the plant pressure drops.

The absence of a sweep gas (see Figure 2b) simplifies the plant arrangement. The oxygen separator is not necessary, and the two condensers are removed as a result of the lower temperature levels achieved at the outlet of the economising section. The recycle of hydrogen is split after the hydrogen separator, ensuring a single-phase stream approaching the H_2 blower.

Each cell of the SOEC employed in the plant features an active area equal to 594 cm^2 – taken as a reference from the available data of the largest solid oxide cells proposed by FuelCell Energy (USA) for SOFC stacks. For each operating condition, the actual required number of cells is obtained via an iterative procedure, with the objective of producing the design hydrogen throughput required by the refuelling station. As far as the inlet flows to the SOEC are concerned, the stream at the fuel electrode is a mixture of steam and hydrogen, with molar fractions of 0.9 and 0.1 respectively; its inlet temperature depends on the temperature of the hydrogen recycle. The sweep consists of steam at 750°C, whose mass flow rate is set to 0.5 kg h^{-1} per cell in the sweep gas case.

Table 2 – Plant input assumptions

Parameter	Unit	Value
ΔT_{ap} gas-gas HEX	°C	30.0
ΔT_{pp} gas-liquid HEX	°C	15.0
Min. temperature at condenser outlet	°C	45.0
Isentropic efficiency of H_2 blower η_{is}	%	70.0
Polytropic efficiency of 3-stage intercooled compressor η_p	%	70.0
Hydraulic efficiency for water pumps η_h	%	75.0

Additional plant input specifications, concerning the considered block units, are summarised in Table 2. It is decided to use the ideal gas equation of state except in the compression train, where the species deviation from ideal gas behaviour is supposed to be more evident. The Peng-Robinson method is chosen accordingly.

For atmospheric operation, the pump discharge pressure is set in order not to run any component in sub-atmospheric condition (the point of minimum pressure is corresponding to the flash separators). For pressurised operation, the pressure at inlet of the SOEC is set at 5 bar, equal to an optimised operating condition suggested by [29].

Solar field design

It is taken into account the integration with a parabolic dish system, which is designed to deliver both electricity $\dot{W}_{el}^{tot}$ and heat $\dot{Q}_{th}^{tot}$ required by the H_2 production plant. Specifically, a multi-dish configuration is chosen, where a number of solar dishes are devoted to the electric supply and they are labelled as “electric dishes”, while at least one solar dish (“thermal dish”), upstream the SOEC unit is devoted to bringing the steam to 750°C, at a pressure range between 1.1-5.2 bar. An air MGT, mounted in correspondence with the focus of the electric dish, constitutes the thermal engine for electricity generation. The MGT operates with an open and recuperated gas turbine cycle, where the working fluid is ambient air [30]. Figure 3 depicts the considered layout of the "electric dish" [31].

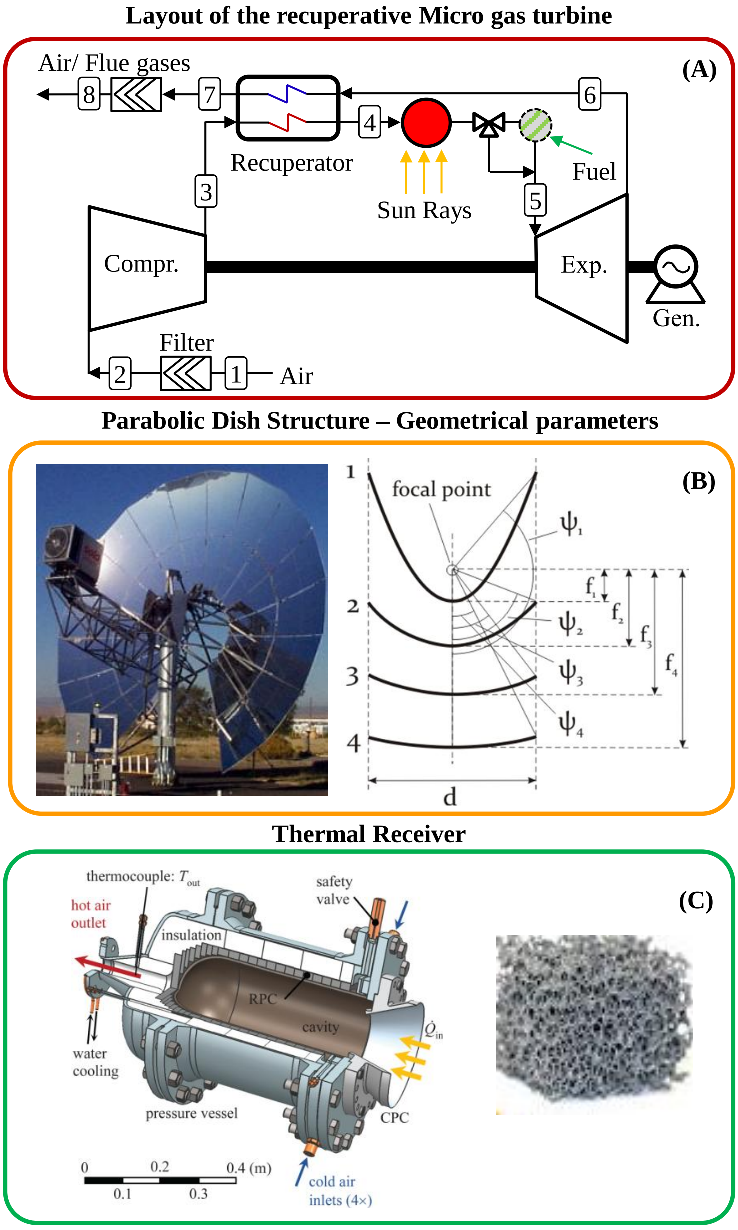
Layout of the recuperative Micro gas turbine

Parabolic Dish Structure – Geometrical parameters

Thermal Receiver

Figure 3 - Scheme of the coupling between MGT and parabolic dish [31]*. The thermal engine is placed at focus of the parabolic mirror. A) Layout of the recuperative Micro Gas Turbine; B) Parabolic dish structure (the effect of rim angle "Ψ" and focal*

distance "f" on mirror shape is highlighted too); C) Scheme of the indirectly-irradiated thermal receiver considered in this study (a detail of reticulated porous ceramic is reported) [32]

Two different design approaches are envisaged:

1. *Solar only*: the solar field is sized to provide the annual energy requirement of the plant (both electric and thermal loads), only by exploiting the solar energy source. For initial analysis, the yearly average conversion efficiency of a stand-alone solar dish is employed in order to obtain an overall hydrogen production efficiency which is representative of the yearly energetic performance of the plant.

   Accordingly, for the electric supply, the useful specific electric energy and the yearly electric energy are determined (Eq. 38 and Eq. 39, respectively), whose ratio returns the dish total aperture area. The useful specific electric energy ($E_{useful,el}$ kWh m^{-2} y^{-1}) is the product between the effective Annual Direct Normal Irradiation ($ADNI_{eff}$ kWh m^{-2} y^{-1}) and the yearly solar-to-electric efficiency of the dish (Eq. 38), as so:

   $$E_{useful,el} = ADNI_{eff} \cdot \bar{\eta}_{s2e} \qquad \textit{Eq. 38}$$

   $ADNI_{eff}$ is obtained by lowering the value of the annual irradiation of the chosen site by two factors: the shade factor (SF), which accounts for the reciprocal shading among the mirrors generated by the sun position variation during each time, and the DNI curtailment, which limits the electric production above 200 W m^{-2}. Over-signed variables represent average yearly values.

   The yearly electric energy (E_{el} kWh y^{-1}) required by the hydrogen production plant is:

   $$E_{el} = \dot{W}_{el}^{tot} \cdot 8760 \qquad \textit{Eq. 39}$$

   Assuming that $\dot{W}_{el}^{tot}$ is the average electric power demand. The procedure is analogous for the thermal dish.

2. *Hybrid*: the system is hybridised using natural gas (NG). The solar field is sized to cover the power input requested by the plant in nominal design condition (DNI 900 W m^{-2}, T_{amb} 35°C, no shading among dishes). The power demand uncovered by the solar field due to lower DNI with respect to the nominal condition, is supplied by natural gas. In particular a hybrid solar MGT is considered, where a burner is placed after the solar absorber and is activated when solar energy is not enough to reach the design turbine inlet temperature (TIT). As far as the thermal demand is concerned, a natural gas fired boiler provides thermal energy in support of the thermal receiver. A boiler efficiency equal to 0.95 is assumed.

The possibility to generate a fully renewable hydrogen, allowed by the first approach, is very fascinating. However, a hybridisation could be regarded as a transition solution, with the advantage that, thanks to natural gas addition, the MGT mounted on the electric dish always works at full load, thus the system can operate at nominal condition for the entire uptime.

Depending on the amount of natural gas employed, a different hybridisation degree (HD) is found. The hybridisation degree reveals the amount of primary energy coming from natural gas, compared to the total inlet primary energy (i.e., solar and natural gas), as reported in Eq. 40.

$$HD = \frac{Q_{ng,MGT} + Q_{ng,boiler}}{Q_{\substack{in,cycle \\ solar+ng}} + Q_{th,solar+ng}} \qquad \textit{Eq. 40}$$

In the preliminary energetic analysis, it is assumed that the system operates continuously by exploiting the natural gas source solely whenever the DNI is below 200 W m^{-2}. Conversely, if the DNI is greater than 200 W m^{-2}, a fraction of energy is provided by the solar source and the complementary fraction is covered by natural gas. This allows to get an upper limit on the yearly performance of the system in hybrid mode, given the target hydrogen throughput. An optimization on the HD will be addressed in the economic/environmental analysis.

Depending on the values of solar dish related efficiencies (solar-to-thermal and solar-to-electric), a ‘base-case’ and an ‘advanced-case’ scenario are defined, as clarified in Table 4. The assumptions on the solar-to-electric efficiency reflect the performance results of a previous study on solarised MGT applied to a parabolic dish [31]. In particular, the ‘advanced-case’ aims at assessing the thermodynamic benefit deriving from the adoption of an MGT endowed with a ceramic expander, allowing a greater maximum temperature (TIT equal to 1100°C, vs. 900°C in the ‘base-case’) to be achieved, with consequent improvement in the cycle efficiency. The value of the diameter of the “electric dishes” D_{el}= 12 m is the result of a trade-off between cost and efficiency and it is suitable for the coupling with commercial MGTs (20-30 kW [33]). The mirror reflectivity is assumed to be equal to 0.94 that has to be intended as a mean annual value that considers soiling and periodical cleanings. The geometric parameters that concur to define the parabolic mirror, namely, the focal length (f) and rim angle (Ψ) are equal to 42° and 7.81 m respectively. In particular, these values can be considered as reasonable as reported in literature [34–36]. A secondary Compound Parabolic Concentrator (CPC), whose outlet diameter is 0.25 m and concentration ratio is equal to 2, is considered too in order to further increase the concentration ratio of the optical system. With Soltrace [37], a Montecarlo raytracing tool widely used in CSP research activity, the optical efficiency, which is the ratio between the absorbed power by the receiver and the solar power at mirror aperture, is estimated to be 0.883.

As regards the thermal receiver, it is based on the indirectly-irradiated concept as proposed by Hischier [32].

Table 3 summarises the main characteristics of the parabolic concentrator that is implemented in the current study. Further information about the performance of the considered optical system can be found in [38].

Table 3 – Solar collector characteristics taken from [38]

Parabolic mirror characteristics	**Unit**	**Value**
Aperture shape	-	Circular
Aperture diameter	m	12.0
Rim angle	°	42.0
Focal length	m	7.81
Mirror reflectivity	-	0.94
Optical errors	mrad	7

The size of the thermal dish is not decided a-priori. Only an upper limit of 400 m^2 on the aperture area is assumed, coherently with the aperture of the ANU Big-Dish prototype described in [39]. The Shade Factor (SF) is assumed and equal to 6.3% for the solar-only case; this will then be checked with yearly calculations on the mutual shading of the dishes.

Table 4 - Base and advanced-case efficiencies for solar only (yearly average values) and hybrid approach (nominal values)

Solar only	Base	Advanced
$\bar{\eta}_{s2e}$ (yearly), %	18.3	26.48
$\bar{\eta}_{s2t}$ (yearly), %	70.0	80.0
Hybrid	Base	Advanced

η_{s2e} (design), %	19.8	28.64
η_{s2t} (design), %	80.0	80.0

Economic modelling

A preliminary economic analysis is performed, considering the hybrid solar field design approach. The main aim is to compare the Levelised Cost of Hydrogen (LCOH) [€ MWh$_{H2}^{-1}$] obtained from the proposed SOEC + dish configuration with other technologies for hydrogen production. Provided a set of economic and financial assumptions, the LCOH is computed as:

$$LCOH = \frac{\bar{C}_{CAPEX} + \bar{C}_{OPEX} + \bar{C}_{tax}}{\bar{E}_{H_2}} \qquad \text{Eq. 41}$$

where, $\bar{C}_{CAPEX}$ is the discounted capital cost, $\bar{C}_{OPEX}$ is O&M annual cost, $\bar{C}_{tax}$ is the cost associated with tax expenditures contribution (computed as 5% of the net income) and $\bar{E}_{H_2}$ is the present value of the total energy output represented by H_2 generation.

The employed cost functions for the current base-case (BS) scenario are summarised in Table 5.

Table 5 – Equipment cost database

Hydrogen generation section			
Item	**Unit**	**Cost function**	**Reference**
Electrolyser	€ m^{-2}	5040.0	[40]
Compressor	€	$16030 \cdot \left(\dot{W}_{el}\ [kW_e]\right)^{0.4411}$	[41]

Condenser	€	$26.4 \cdot 10^{6} \cdot \left(\frac{\dot{Q}_{cond}[\mathrm{MW}_{th}]}{470}\right)^{0.67}$	[42]
Heat exchangers	€	$2.78 \cdot 10^{3.6788+0.4412\log(A_{HEX}\,[\mathrm{m}^2])}$	[20]
Pump	€	$808.19 \cdot \left(\frac{\dot{W}_{pump}[\mathrm{kW}]}{0.98}\right)^{0.2724}$	[41]

Solar field section

Item	**Unit**	**Cost function**	**Reference**
Mirror	€ m^{-2}	250	[38]
Land	€ m^{-2}	17.7	[28]
Receiver	€ kW_{th}^{-1}	135	[38]
Hybrid MGT	€ kW^{-1}	600	[43][1]
NG boiler	€ kW_{th}^{-1}	15	[43]

A long-term scenario (LS) is considered, in which electrolyser, mirror and thermal receiver experience a major cost reduction: 2520 € m^{-2}, 175 € m^{-2}, 67.5 € kW_{th}^{-1} are the LS specific costs, respectively. The specific cost of natural gas is site dependent; therefore, in this study its industrial price for California state is considered equal to 0.2867 € kg^{-1} (i.e., 6.17 € GJ^{-1}) [44].

---

[1] As underlined in [30], the specific cost is strongly influenced by the market size.

RESULTS AND DISCUSSION

Model validation

The SOEC model is validated using the experimental data presented by Menon et al., [5] as reference data. Experimental tests were performed by [24] on a planar button SOEC produced at Risø National Laboratory, constituted by a NiO/YSZ fuel electrode, a YSZ electrolyte and a LSM/YSZ sweep electrode. Input data to the model are summarised in Table 1. Note that since the reference experimental data are relative to a button cell in isothermal condition (T_{PEN} is constant and uniform), the same assumption is employed in this model.

Three polarization curves performed at different temperatures and atmospheric pressure are calibrated, as depicted in Figure 4. A good agreement is found between numerical results and measured data, with the exception of a slight voltage overestimation at intermediate temperatures. Consequently, the model input parameters succeed in matching the simulated cell performances with the real one.

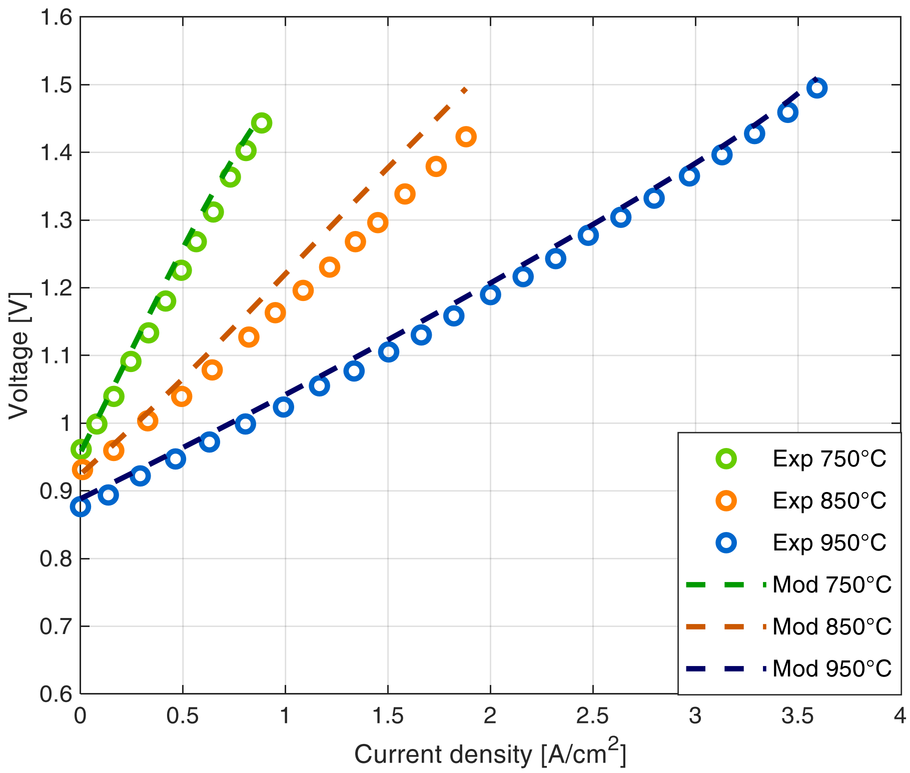

Figure 4 - Model validation. Dashed lines are the modelled polarization curves; experimental data from Jensen et al., 2007 [24] *are marked with dots*

Model results

The model is used to explore the utilisation of diverse sweep gas type (i.e., air, steam). The results show that the deployment of non-oxygen-containing species could reduce the Nernst potential – thus reducing the cell voltage – at a given current density. This brings about a higher SOEC electric efficiency, defined as the ratio of the hydrogen power output (LHV-based) to the electric consumption (see Eq. 7). In case steam is employed as sweep gas, the lower Nernst potential and the high heat capacity allow widening the operation range in endothermic mode, with an advantageous decrement of the electric power absorbed by the SOEC itself.

The derivation of cell internal profiles (i.e., temperature and current density) reveals how the evolution of polarization losses and their magnitude directly reflects the current density distribution and the thermal characteristic of the SOEC. Figure 5a shows the temperature profiles relative to the anodic and cathodic streams and to the PEN structure, at two different values of current density. At low current density, the behaviour of the SOEC is endothermic because the endothermic nature of the electrolysis reaction prevails over the heating associated with polarization losses. As a result, a decrease in the temperatures is observed. A higher current density contributes to boosting irreversibilities within the cell, therefore both streams, as well as the electrode-electrolyte assembly are heated up by the cell internal heat generation.

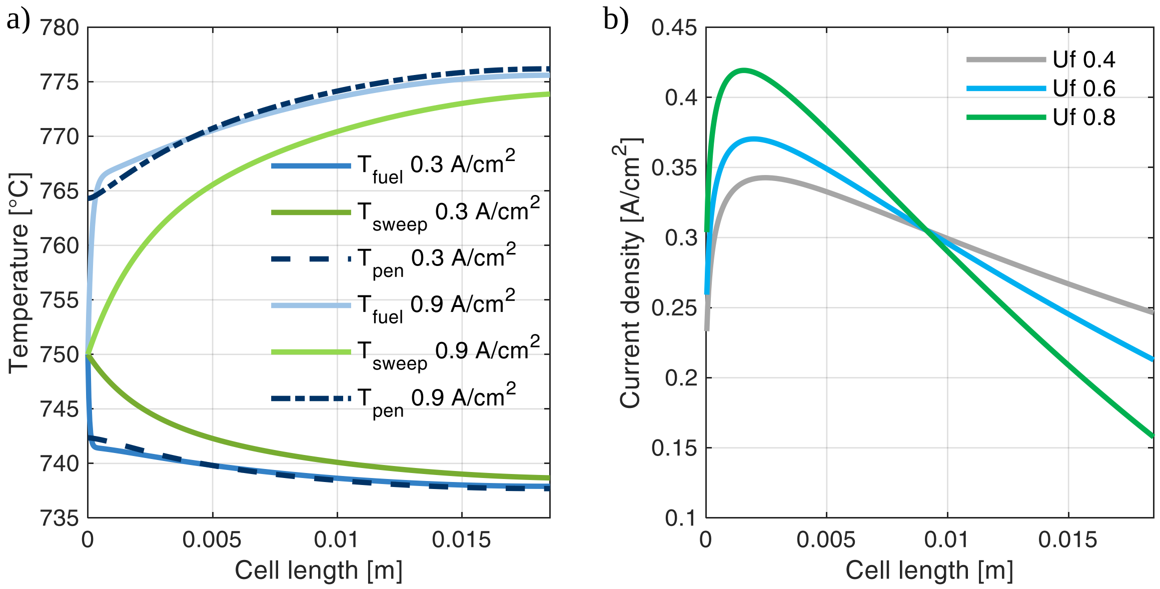

Figure 5 - (a) Temperature profiles of PEN, fuel and sweep streams at 0.3 A cm^{-2} and 0.9 A cm^{-2} - T_{in} streams 750°C, U_f = 0.6, sweep mass flow rate 0.01 kg/h; (b) Current density profiles and variation with steam utilization

Figure 5b shows that the current density profile features a peak that lays within the first 20% of the channel length, corresponding to the maximum steam conversion point. Subsequently, a decreasing trend is observed coherently with the reduction of steam concentration at the fuel side from inlet to outlet. At higher steam utilisation U_f (see Eq. 42) a larger amount of hydrogen is generated at the inlet of the cell.

$$U_f = \frac{\dot{n}_{H_2O}^{prod}}{\dot{n}_{H_2O}^{in}} = \frac{\frac{jA}{2\mathcal{F}}}{x_{H_2O} \cdot \dot{n}_{in}} \qquad \textit{Eq. 42}$$

A sensitivity analysis is also performed on the sweep gas flow rate and a map of the cell net thermal flux is obtained (Figure 6a), which clearly identifies the different thermal operating conditions of the SOEC. The iso-line corresponding to $\dot{Q}_{SOEC} = 0\,kW$ represents the thermoneutral condition, featuring a cell voltage equal to 1.285 V. This condition occurs progressively at higher current densities as steam flow rate, employed as sweep gas, increases; at high sweep flow rate, a more rapid rise of the heat generated by polarization losses leads to a slight reduction in the current density at the thermoneutral point. On the right hand side of the map, the cell functioning is above the thermoneutral voltage; $\dot{Q}_{SOEC}$ becomes negative and the cell needs to be cooled in order to be isothermal. Conversely, on the left hand side, the cell shows an endothermic behaviour; therefore, it requires a thermal input to carry out the electrolysis at constant temperature. A maximum in the net thermal flux is found for each sweep gas flow rate considered.

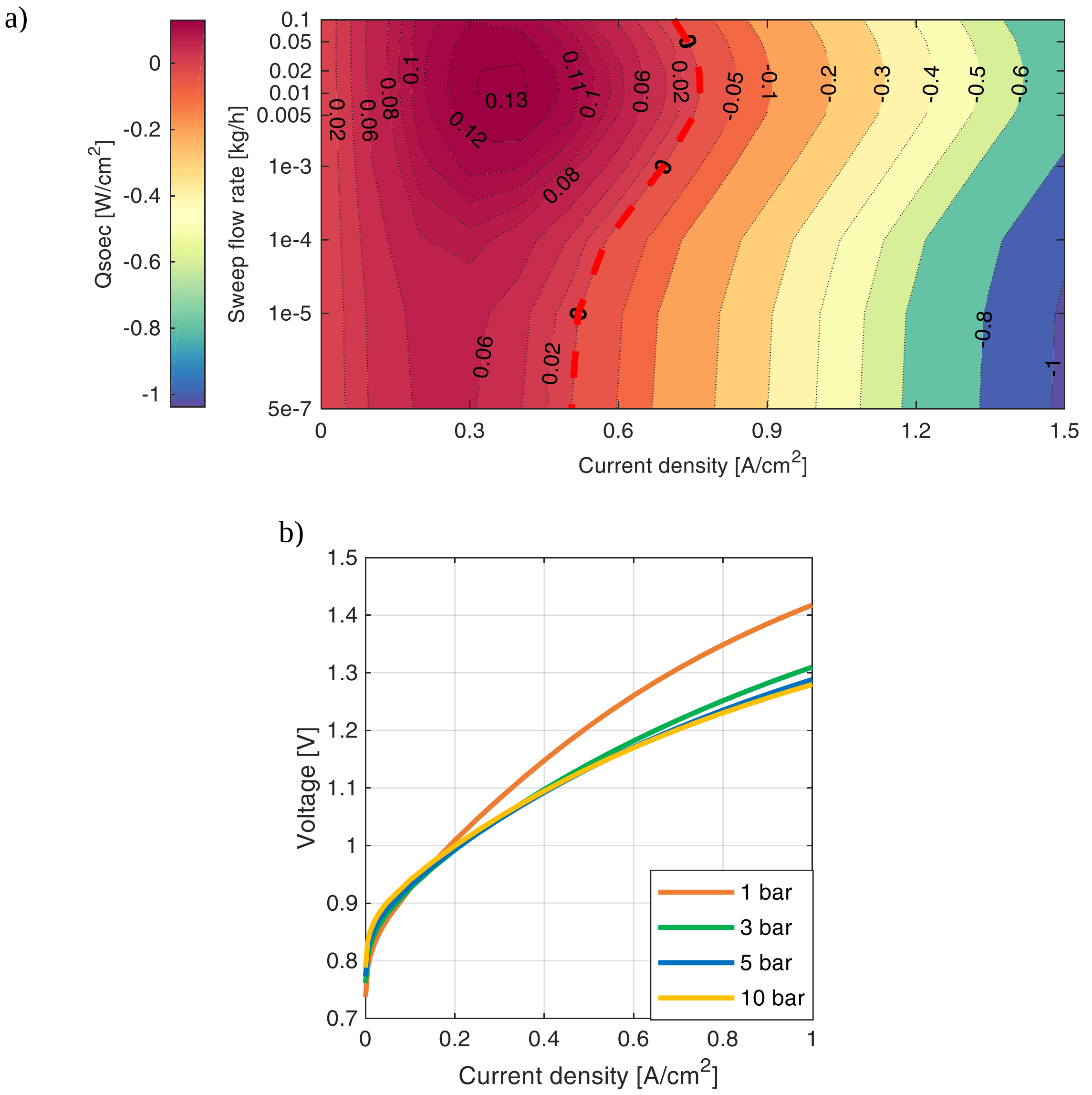

Figure 6 - (a) Map of Q_{SOEC} at 750°C; (b) Polarisation curves at different values of pressure

Finally, pressurised cell operation is simulated. Results (Figure 6b) show that polarization curves at high pressure cross the one at atmospheric pressure, meaning that at higher current density, the decrease in the overpotentials prevails over the Nernst voltage increase and thus succeeds in reducing the cell voltage. Therefore, operation at high pressure (>3 bar) is particularly advantageous when working at high current densities. These results confirm those already obtained by Bernadet et al., [29].

Plant results

Atmospheric operation

The number of cells needed for different values of nominal current density is showed in Figure 7. At increasing j, the hydrogen production rate of each cell increases, so a lower number of cells is required to meet the hydrogen throughput target. The trend of plant power requirements, both electric $\dot{W}_{el}^{tot}$ and thermal $\dot{Q}_{el}^{tot}$ are evaluated as function of current density and steam utilization. The former scales with current density because the SOEC absorbs more electricity to increase its hydrogen production rate. On the other hand, the electric demand decreases with increasing steam utilisation factor, because the equipment (mainly the intercooled compressor of H_2) manages a lower water/steam flow rate and therefore consumes less electricity. Vice versa, the thermal demand is minimised at the highest current densities. In fact at high j, due to the exothermic behaviour of the SOEC, the outlet streams from the sweep and fuel channels are hotter and more heat can be transferred to the feed water in the heat exchange section. Therefore, the stream going to the solar section is characterized by a higher vapour fraction. The lowest power consumption occurs at the highest steam utilisation factor because of the lower amount of fluid that the plant is processing.

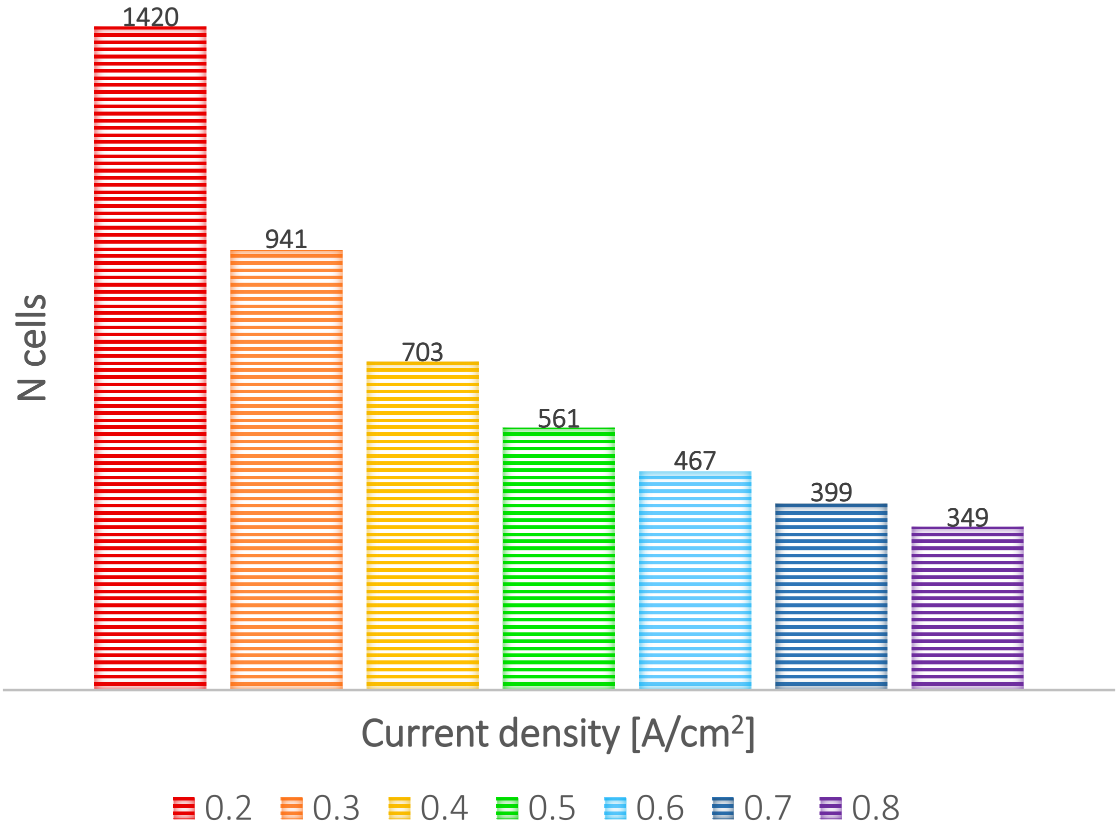

Figure 7 - Number of cells obtained for each current density. Values refer to the 60% U_f simulation case.

Solar only

The solar to hydrogen efficiency, whose design map is provided in Figure 8a, is expressed as:

$$\eta_{sun-to-H_2} = \frac{m_{H_2} LHV_{H_2}}{\frac{E_{el}^{tot}}{\bar{\eta}_{s2e}^{tot}} + \frac{Q_{th}^{tot}}{\bar{\eta}_{s2t}^{tot}}} \qquad \text{Eq. 43}$$

where, $\bar{\eta}_{s2e}^{tot}$ and $\bar{\eta}_{s2t}^{tot}$ are the yearly averaged conversion efficiencies of the electric dish and thermal dish respectively, based on the effective Annual Direct Normal Irradiation. This efficiency is representative of the yearly energy performance of the plant.

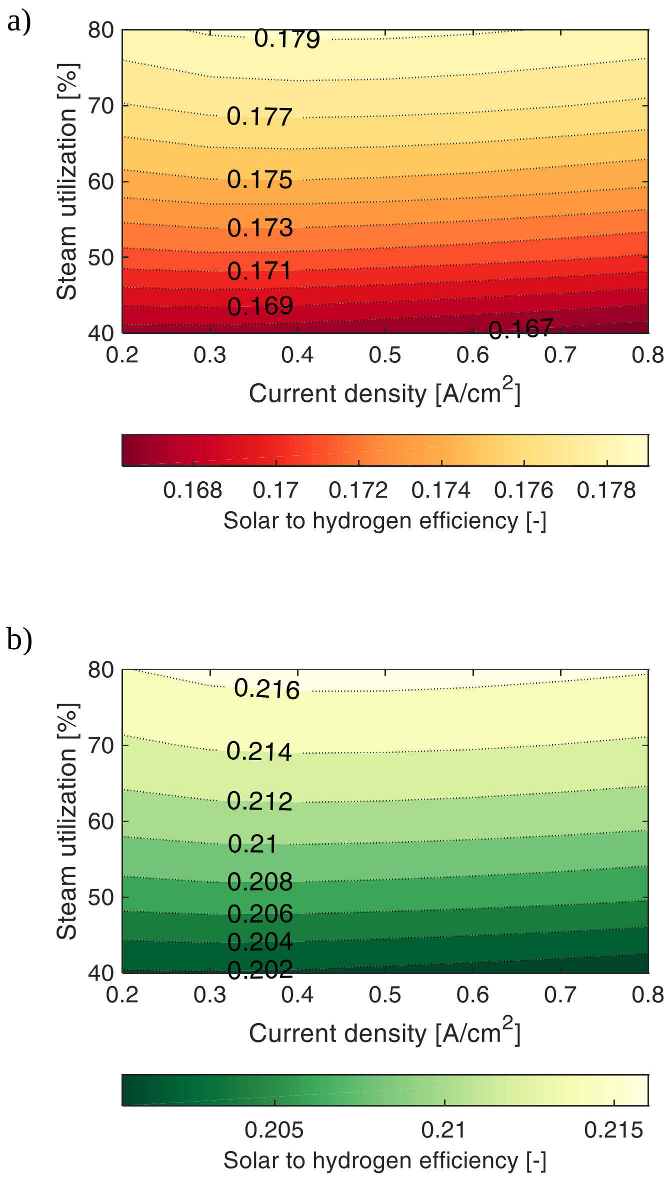

Figure 8 - (a) Yearly solar to hydrogen efficiency design map for solar only advanced case; (b) Nominal solar to hydrogen efficiency design map for hybrid advanced case - no sweep gas, atmospheric operation

Coherently with the previous discussion, best efficiency points appear at the highest steam utilisation. A maximum of 12.5% is found at a medium value of current density (0.4 A cm^{-2}) for the ‘base-case’ scenario, because the contribution of electric power at the denominator weighs more than the thermal power. At high current density, the increment in the electric power requirement slightly prevails over the thermal power reduction. In an ‘advanced-case’ scenario, an increase of 30% is observed compared to the ‘base-case’ values: a maximum η_{s2H_2} of 17.9% is achieved, as visualized in Figure 8a,

Hybrid

The solar-to-hydrogen efficiency is written in an analogous way as in Eq. 43, but substituting the electric and thermal efficiencies with those for the nominal design condition (see Table 4). The best efficiency point is again found at 0.4 A cm^{-2}, 80% U$_f$, with a value of 15.2% in the ‘base-case’ and of 21.7% in the ‘advanced-case’, as can be observed in Figure 8b. On a yearly averaged basis, a hybrid efficiency can be defined as in Eq. 44.

$$\bar{\eta}_{hybrid} = \frac{m_{H_2} LHV_{H_2}}{E_{sun} + Q_{fuel}} \qquad \text{Eq. 44}$$

At the denominator, two contributions appear: the first being the annual solar energy, the second the annual fuel energy associated to the natural gas consumption. For the best efficiency point, the resulting hybrid average annual efficiency is 18.4% in the ‘base-case’ and 26.4% in the ‘advanced-case’.

In the sweep gas case, the need to heat the steam employed as sweep gas leads to a greater duty from the thermal solar dish section. In fact, in the cooling process of the hot streams exiting the SOEC, the latent heat is lost in the condensers and needs to be delivered again, in part by the thermal dish, to the liquid water entering the process. Consequently, lower solar to hydrogen efficiencies are obtained: 13.9% that raises to 19.2% in the hybrid ‘advanced-case’.

Pressurised operation

Similar design performance maps are derived for operation at 5 bar (omitted for brevity), from which it is possible to appreciate an improvement in the solar to hydrogen efficiency. The reason is that not only the electrochemical performance of the SOEC itself is enhanced, but also the plant thermodynamic performance is improved; in fact, the electricity consumption linked to the compression blocks reduces and the evaporation of water is thermodynamically favoured due to the reduced latent heat for phase change.

For the well performing no sweep gas case, the trade-off between the electric power increase and the thermal power decrease at high current density leads to locate the best solar-to-hydrogen efficiency point at 0.6 A cm^{-2}. The following Table 6 summarises the resulting values of solar efficiency for the best efficiency point. Also, the needed number of electric dishes is specified (fixing a diameter of 12 m) while only one thermal dish is sufficient to fulfil the heat duty required from the plant.

Table 6 – Summary of power balances, solar efficiencies and number of electric dishes for pressurised solar-only and hybrid approach in 'base-case' and 'advanced-case' scenarios without sweep gas. Values refer to the highest efficiency point, hydrogen production 150 kg day^{-1}.

Electric power [kW]		
SOEC	219	
H_2 compressor	19.1	
O_2 compressor	8.8	
Pump, H_2 blower and aux.	0.35	
Thermal power [kW]		
Thermal dish total duty	38.2	
Solar only	**Base**	**Advanced**

$\bar{\eta}_{sun-to-H_2}$ (yearly) [%]	13.2	18.9
N° electric dishes	40	28
Solar field total aperture area [m^2]	4703	3324
Hybrid	**Base**	**Advanced**
$\eta_{sun-to-H_2}$ (design) [%]	16.1	22.9
η_{hybrid} [%]	18.5	26.5
HD [%]	62.1	62.5
N° electric dishes	13	9
Solar field total aperture area [m^2]	1523	1071

Figure 9 shows an example of the solar field layout related to the hybridized solution with the 'advanced-case' SMGT assumptions. In particular the depicted scene refers to zenith angle (θ_z) and azimuth angle (γ) equal to 65° and 125° respectively while the shade factor is 5.31%. The central dish, which satisfies the SOEC thermal load, is surrounded by nine dishes equipped with a MGT that provides the electricity to the SOEC. This configuration mimics a flower where the "thermal dish" represents the pistil.

It is worth to underline that the solar field layout proposed in Figure 9 has to be considered as a preliminary solution that assumes no obstacles (i.e. existing buildings, trees etc.) and no boundaries of available land. The optical optimization of parabolic dishes layout, which aims to maximise the available DNI, will be part of future activities.

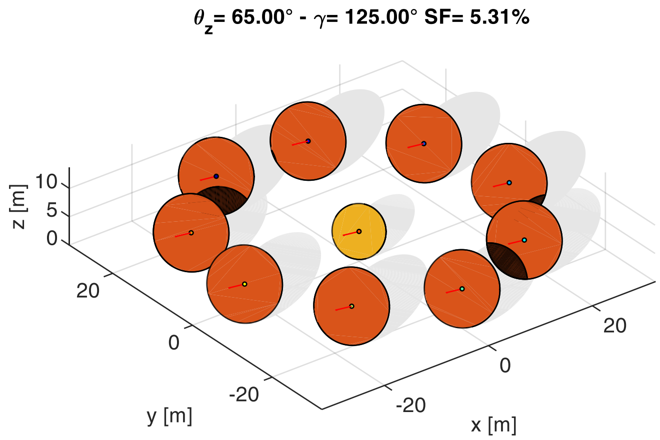

Figure 9 - 3D view of the solar field configuration. Sun position in the sky is defined by the zenith angle (θ_z) and azimuth angle (γ) equal to 65° and 125° respectively. Shade factor is 5.31%.

Economic and environmental assessment

Table 7 summarises the results of the economic and environmental assessment. Under the hypothesis of no production for DNI lower than 200 W m^{-2}, the equivalent operating hours are about 3700 h y^{-1} for the presented cases. Different cases labelled A, B, C and D are presented, which differ in terms of current density, use of sweep gas and pressurisation. In BS, the lowest values of LCOH occur for cases B and D, confirming that operation under pressure is a promising technical solution for making the technology more economically viable. Case B takes advantage of the reduced plant complexity which characterises the no-sweep layout, whereas in case D, the use of a larger number of components is offset by the higher operating current density.

The hybrid plant configurations are also evaluated in terms of their $CO_{2,eq}$ emissions, due to the consumption of natural gas. The emissions are calculated by summing the overall CO_2 emissions (for both electric and thermal power generation) during the yearlong operation of the system by multiplying the hourly natural gas consumption by its emission factor (i.e., 2.60 $kg_{CO2}\ kg_{NG}^{-1}$).

Table 7 – Economic analysis results

	Units	**A**	**B**	**C**	**D**
Sweep gas				●	●
Pressurised			●		●
j	$A\ cm^{-2}$	0.4	0.6	1.0	1.0
U_f	%	80.0	80.0	80.0	80.0
η_{hybrid}	%	15.2	16.0	13.8	14.8
HD	%	18.4	18.4	18.5	18.5
e_{CO2}	$kg_{CO2}\ kg_{H2}^{-1}$	6.2	5.9	6.9	6.4
BS cost					
TDP	$M€$	1.110	0.976	1.146	1.066
$C_{O\&M,fixed}$	$M€\ y^{-1}$	0.054	0.045	0.048	0.046
$C_{O\&M,var}$	$M€\ y^{-1}$	0.016	0.015	0.018	0.016
LCOH	$€\ kg^{-1}$	9.0	7.85	9.1	8.5

LS cost					
TDP	$M€$	0.818	0.730	0.899	0.833
LCOH	$€\,kg^{-1}$	6.6	5.9	7.2	6.7

The major contribution to the total investment cost is from the solar dish section (above 70%), being the mirrors and the thermal receiver the dominant cost items. In the LS, the LCOH decreases, achieving a minimum value of 5.93 € kg^{-1} for case B. Capital cost accounts for about 68% of the total LCOH, followed by the fixed O&M costs (19%), while variable O&M costs represent around 10% of the final cost of hydrogen. The tax portion is minor with respect to the other contributions.

Discussion

From an efficiency standpoint, the system results to be competitive if compared to other solar hydrogen technologies, such as PEM coupled with photovoltaics [45,46], or SOEC coupled to a solar tower system [47], as reported in Table 8. In addition, the cost of hydrogen in this study is in line with the outcomes present in literature. However, it should be reminded that the condition reported in this study is a natural gas hybrid configuration, which is characterised by a CO_2 emission footprint higher than any of the other renewable alternatives.

Table 8 - Comparison of solar-to-hydrogen efficiency and LCOH for different hydrogen production technologies

System	$\eta_{sun-to-H_2}$ **[%]**	**H_2 yield**	$LCOH$	**Reference**
SOEC + Parabolic dish (NG - hybrid)	11.4 – 16	150 kg d^{-1}	5.9-9.1 € kg^{-1}	This study

SOEC + Solar Tower	10.6	400 kg d^{-1}	8.2 \$ kg^{-1}	[20]
SOEC + PV	6.3	400 kg d^{-1}	8.0 \$ kg^{-1}	[20]
SOEC + PV + Solar Tower	9.9-12.7	400 kg d^{-1}	6.3 \$ kg^{-1}	[20,48]
SOEC + PV + Parabolic trough	NA	NA	5.23 \$ kg^{-1}	[49,50]
PEM + PV grid assisted	9.76	≈417 kg h^{-1}	6.1 \$ kg^{-1}	[45]
PEM + PV directly coupled	11.6	≈7 kg y^{-1}	7.32 € kg^{-1}	[49,51]
PEM + PV/thermal hybrid	15-17.3	NA	NA	[46]
ALK + PV grid assisted	7.4 – 9.3	0.5 kg d^{-1}	6.66 € kg^{-1}	[49,52]
Steam methane reforming			1.5-2.6 \$ kg^{-1}	[53]

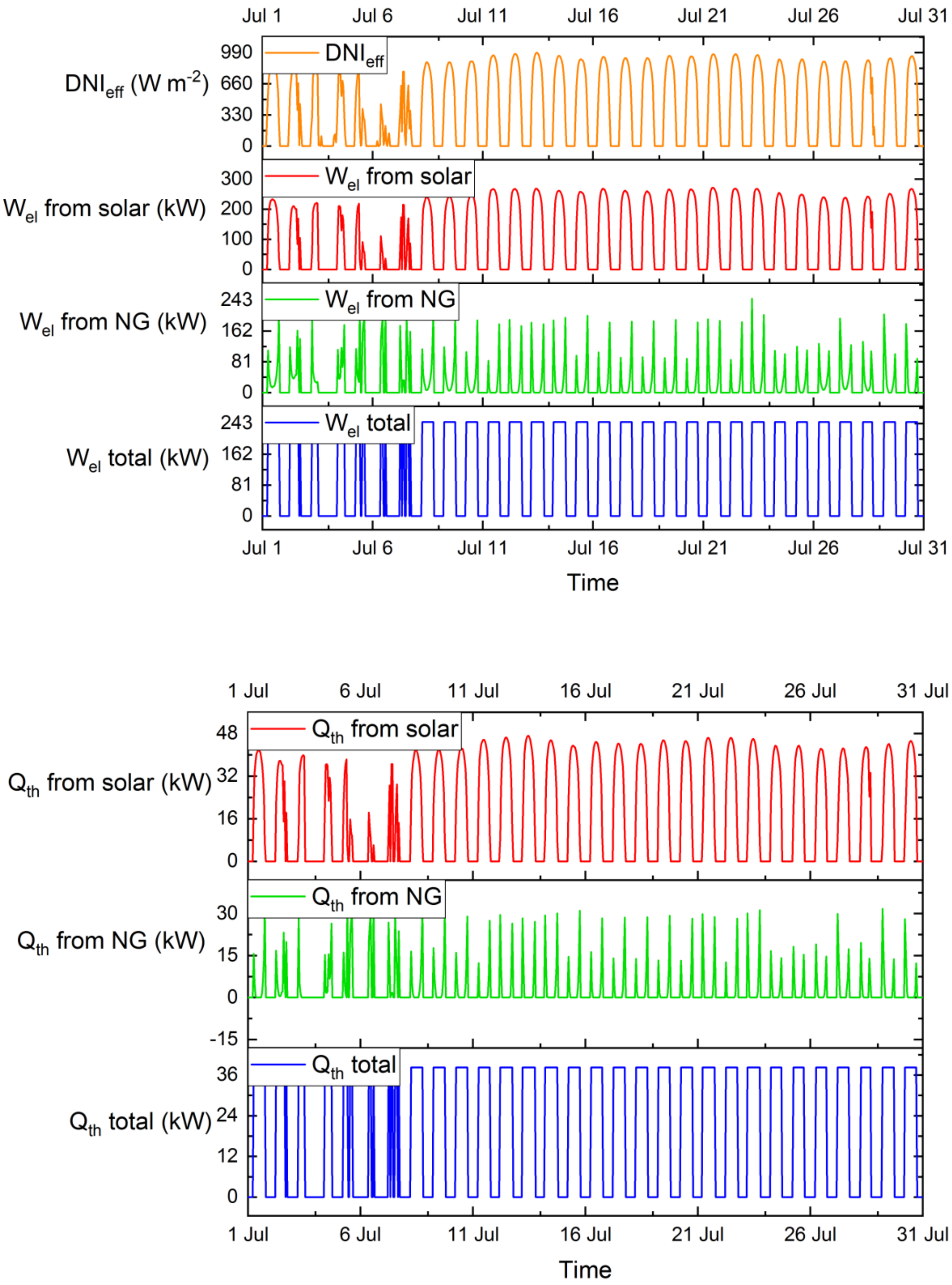

Figure 10 - Time profile variation of electric power (a) and thermal power supply (b) on behalf of natural gas and solar sources in hybrid mode for July

Despite being still not competitive with respect to conventional steam methane reforming (SMR), which exhibits the lowest hydrogen production costs to date, the proposed SOEC+CSP hybrid system is outperforming on the level of emissions. In fact, it is found that the specific CO_2 emissions of pressurised case without sweep flow (case B) are 5.9 $kg_{CO2}\ kg_{H2}^{-1}$, which is lower if compared to a typical SMR (i.e., ≈ 10 $kg_{CO2}\ kg_{H2}^{-1}$ [54]); by this point of view, although the economic gap vs. a SMR is wide, the introduction of a carbon tax could help the system economics. The results are explained by the substantial use of solar energy, leading to a hybridisation degree of approximately 18%. In Figure 10, it is possible to appreciate the system operation in hybrid mode for a one-month representative timeframe (e.g., July), and the share of natural gas and solar sources for the supply of the target energy requirement.

Keeping the same solar field size and allowing the system to operate at higher capacity factor by increasing natural gas input, it turns out that 32% hybridisation degree is the upper limit in order to not exceed the reference Steam Methane Reforming (SMR) emissions; in such circumstances, the LCOH drops to 6.9 € kg^{-1} in BS and 5.3 € kg^{-1} in LS (case B), while the equivalent hours raise to 4531 h y^{-1}. However, the solution is not competitive vs. a SMR given the higher complexity and the same emission results.

Finally, to gain a better insight on the link among emission, hybridisation and LCOH as function of the solar field area, a sensitivity analysis is performed, whose outcomes are visualized in Figure 11. It is assumed that the electric energy produced in excess by the solar field is injected in the grid and valorised at 66.8 € MWh_{el}^{-1} [44]. In this analysis, if excess thermal energy remains – downstream the heat recovery section – low temperature heat dissipation occurs.

It is noticeable that, fixing the system capacity factor, when the solar field segment is progressively enlarged, the hybridisation degree reduces as well as the corresponding CO_2 emissions, but this would come at an increased LCOH. In the end, it inevitably emerges a trade-off between energetic sustainability of the system and economic impact on the cost of hydrogen.

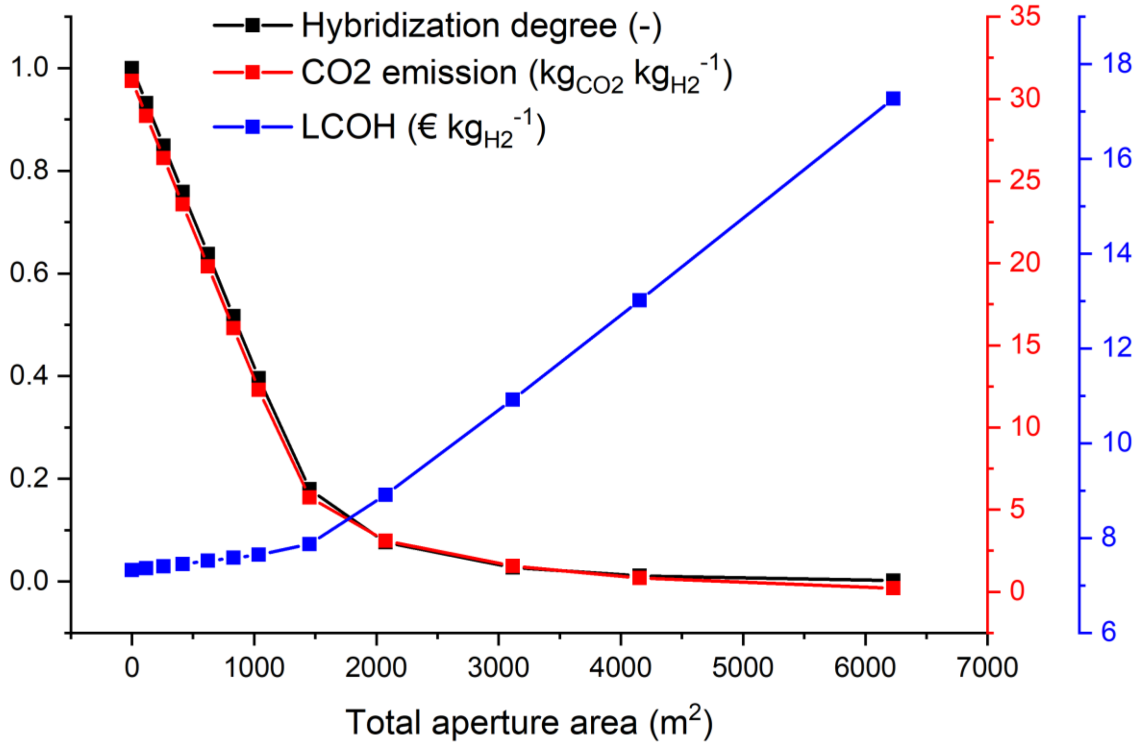

Figure 11 - Trends of LCOH, CO_2 emissions and HD as function of the solar field area in BS case – no sweep, pressurised. Assumptions: no production for DNI < 200 W m^{-2}, excess electric energy from sun is injected in the grid

CONCLUSION

In this paper, the coupling between a solid oxide electrolysis cell and a parabolic dish system for solar hydrogen production is investigated. Focusing on solid oxide electrolysis cell modelling, a 1D cell model is defined and subsequently applied to generate useful results for any relevant electrochemical and thermodynamic variable, enabling the discussion of the effects of different operating conditions on the internal solid oxide electrolysis cell behaviour.

The overall plant model is developed using Aspen Plus, in which the solid oxide electrolysis cell unit is incorporated as a sub-model. In pursuit of solar to hydrogen efficiency optimization, different operating nominal conditions of the solid oxide electrolysis cell within the plant are examined, in terms of pressure, current density, steam utilization and sweep gas flow rate, with the objective to produce a hydrogen throughput of 150 kg d^{-1}. It is found that the overall system conversion efficiency could be enhanced by (1) sweep gas minimization, (2) high steam utilization, (3) pressurization, (4) current density values in the range 0.4-0.6 A cm^{-2} (for the no sweep gas case), corresponding to a voltage for each cell of about 1.3 V.

The best solar to hydrogen efficiency is found to be 18.9%, on a yearly averaged basis, corresponding to the no sweep pressurized scenario. Within the hybrid approach (using natural gas to integrate the solar energy in periods at low direct normal irradiation), a solar-to-hydrogen efficiency of 22.9% is attained in design conditions, leading to a hybrid efficiency of 26.5%, on a yearly basis.

Results of the economic analysis showed that pressurization and high current density operation together move in the direction of a more affordable solar hydrogen generation. However, the resulting value of levelised cost of hydrogen (5.9 € kg^{-1}) confirms that the proposed system is still not competitive if compared to steam reforming hydrogen production, mainly due to the minor technological maturity of the parabolic dish system; nevertheless, it is in line with other solar hydrogen solutions.

Specific carbon dioxide emissions are around 6 $kg_{CO2}\ kg_{H2}^{-1}$ for the presented cases (corresponding to a hybridisation degree of 18%), which are lower than typical values from steam methane reforming (≈ 10 $kg_{CO2}\ kg_{H2}^{-1}$).

Off-design analysis, that will be the subject of future works, could deepen the feasibility assessment of a totally renewable solar hydrogen production, by examining the coupling of the solar energy distribution with typical hydrogen demand profiles. Besides, the incorporation of a thermal energy storage and the possible effects of a carbon tax shall be investigated. In addition, a Well-to-Wheel cost analysis, which would include the proposed system configuration as hydrogen production step in the overall hydrogen supply chain will be considered for future analysis.

NOMENCLATURE

Symbols

A	Cell active area / m^2
c_p	Specific heat capacity / $kJ\ kg^{-1}\ K^{-1}$
C	Molar concentration / $mol\ m^{-3}$
C_{CAPEX}	Investment cost / M€
$C_{O\&M,fixed}$	Fixed Operation and Maintenance cost / M€
D	Diffusivity / $cm^2\ s^{-1}$
E_{act}	Activation energy / $kJ\ mol^{-1}$
E_N	Nernst voltage / V
f	Focal length / m
$\mathcal{F}$	Faraday constant / 96485 $C\ mol^{-1}$
L	Cell length / m
h	Molar enthalpy / $J\ mol^{-1}$
H_{ch}	Channel height / m
MM	Molar mass / $kg\ kmol^{-1}$
q_{SOEC}	Net thermal flux / $W\ cm^{-2}$
$\dot{Q}$	Thermal power / kW

r	Reaction rate / $mol\ s^{-1}\ m^{-2}$
r_{pore}	Average pore radius / μm
$\mathcal{R}$	Universal gas constant / 8.314 $J\ K^{-1} mol^{-1}$
R_{eq}^{tot}	Equivalent total resistance / Ωm^2
T	Temperature / $°C$
U_f	Steam utilisation factor / -
V	Cell voltage / V
W	Cell width / m
$\dot{W}$	Electric power / kW
j	Current density / $A\ m^{-2}$
j_0	Exchange current density / $A\ m^{-2}$
k	Thermal conductivity / $W\ m^{-1}\ K^{-1}$
$\dot{m}$	Mass flow rate / $kg\ s^{-1}$
$\dot{n}$	Molar flow rate / $mol\ s^{-1}$
p	Pressure / bar
p^*	Equilibrium pressure / atm
p_0	Standard pressure / 1 atm
t	Time / s
u	Velocity / $m\ s^{-1}$
x	Molar fraction / -

z	Number of charge carriers transferred / mol

Greek symbols

β	Symmetry factor / -
γ	Pre-exponential factor / $A\ m^{-2}$
δ	Thickness / μm
ΔG	Gibbs free energy change / $kJ\ mol^{-1}$
ΔH	Enthalpy change / $kJ\ mol^{-1}$
ΔS	Entropy change / $kJ\ mol^{-1}K^{-1}\eta_{act}$ Activation overpotentials / V
η_{conc}	Concentration overpotentials / V
η_{ohm}	Ohmic overpotentials / V
ϵ	Emissivity / -
η_{hybrid}	Hybrid efficiency / %
$\eta_{sun-to-H_2}$	Solar to hydrogen efficiency / %
η_{s2e}	Solar to electric efficiency / %
η_{s2t}	Solar to thermal efficiency / %
ν	Stoichiometric coefficient / -
ρ	Density / $kg\ m^{-3}$
σ	Ionic/Electric conductivity / $S\ m^{-1}$
ϕ	Electrodes porosity / -
τ	Electrodes tortuosity / -

Ψ	Rim angle / °

Acronyms/abbreviations

ALK	Alkaline Electrolyser
CSP	Concentrated Solar Power
HEX	Heat Exchanger
DNI	Direct Normal Irradiance / $W\ m^{-2}$
LCOH	Levelised Cost Of Hydrogen / € kg^{-1}
LHV	Lower heating Value / $MJ\ kg^{-1}$
LSCF	Lanthanum Strontium Cobalt Ferrite
LSM	Lanthanum Strontium Manganite
MGT	Micro Gas Turbine
NG	Natural Gas
ORC	Organic Rankine Cycle
PEM	Polymer Electrolyte Membrane
PEN	Positive-Electrolyte-Negative structure
SF	Shade Factor
SMR	Steam Methane Reformer
SOEC	Solid Oxide Electrolysis Cell
TDP	Total Direct Plant cost / $M€$
TIT	Turbine Inlet Temperature / $°C$

TPB	Triple Phase Boundary
YSZ	Yttria Stabilised Zirconia

Subscripts

ap	Approach point
pp	Pinch point
b	Gas bulk property
l	Electrodes layer property
ch	Channel-related term
el	Electricity-related term
th	Thermal-related term
0	Standard conditions
cell	cell-related term
th	thermoneutral condition
fu	fuel electrode
sw	sweep electrode
int	interconnect
red	reduction
ox	oxidation

Superscripts

$-$	year averaged value

·	power value
prod	produced quantity

REFERENCES

[1] S. Timmerberg, M. Kaltschmitt, Hydrogen from renewables: Supply from North Africa to Central Europe as blend in existing pipelines – Potentials and costs, Appl. Energy. 237 (2019) 795–809. doi:10.1016/j.apenergy.2019.01.030.

[2] S. Samsatli, N.J. Samsatli, The role of renewable hydrogen and inter-seasonal storage in decarbonising heat – Comprehensive optimisation of future renewable energy value chains, Appl. Energy. 233–234 (2019) 854–893. doi:10.1016/j.apenergy.2018.09.159.

[3] International Energy Agency (IEA), Technology Roadmap Hydrogen and Fuel Cells, 2015. doi:10.1007/SpringerReference_7300.

[4] J. Udagawa, P. Aguiar, N.P. Brandon, Hydrogen production through steam electrolysis: Model-based steady state performance of a cathode-supported intermediate temperature solid oxide electrolysis cell, J. Power Sources. (2007). doi:10.1016/j.jpowsour.2006.12.081.

[5] V. Menon, V.M. Janardhanan, O. Deutschmann, A mathematical model to analyze solid oxide electrolyzer cells (SOECs) for hydrogen production, Chem. Eng. Sci. 110 (2014) 83–93. doi:10.1016/j.ces.2013.10.025.

[6] V. Menon, Q. Fu, V.M. Janardhanan, O. Deutschmann, A model-based understanding of solid-oxide electrolysis cells (SOECs) for syngas production by H2O/CO2 co-electrolysis, J. Power Sources. (2015). doi:10.1016/j.jpowsour.2014.09.158.

[7] D. Ferrero, A. Lanzini, P. Leone, M. Santarelli, Reversible operation of solid oxide cells under electrolysis and fuel cell modes: Experimental study and model validation, Chem. Eng. J. 274 (2015) 143–155. doi:10.1016/j.cej.2015.03.096.

[8] A.A. AlZahrani, I. Dincer, Modeling and performance optimization of a solid oxide

electrolysis system for hydrogen production, Appl. Energy. 225 (2018) 471–485. doi:10.1016/j.apenergy.2018.04.124.

[9] X. Xing, J. Lin, Y. Song, Q. Hu, Y. Zhou, S. Mu, Optimization of hydrogen yield of a high-temperature electrolysis system with coordinated temperature and feed factors at various loading conditions: A model-based study, Appl. Energy. 232 (2018) 368–385. doi:10.1016/j.apenergy.2018.09.020.

[10] P. Kazempoor, R.J. Braun, Model validation and performance analysis of regenerative solid oxide cells for energy storage applications: Reversible operation, Int. J. Hydrogen Energy. 39 (2014) 5955–5971. doi:10.1016/j.ijhydene.2014.01.186.

[11] P. Kazempoor, R.J. Braun, Model validation and performance analysis of regenerative solid oxide cells: Electrolytic operation, Int. J. Hydrogen Energy. (2014). doi:10.1016/j.ijhydene.2013.12.010.

[12] C.H. Wendel, Z. Gao, S. a. Barnett, R.J. Braun, Modeling and experimental performance of an intermediate temperature reversible solid oxide cell for high-efficiency, distributed-scale electrical energy storage, J. Power Sources. 283 (2015) 329–342. doi:10.1016/j.jpowsour.2015.02.113.

[13] M. Ni, M.K.H. Leung, D.Y.C. Leung, A modeling study on concentration overpotentials of a reversible solid oxide fuel cell, J. Power Sources. (2006). doi:10.1016/j.jpowsour.2006.09.024.

[14] Y. Wang, A. Banerjee, L. Wehrle, Y. Shi, N. Brandon, O. Deutschmann, Performance analysis of a reversible solid oxide cell system based on multi-scale hierarchical solid oxide cell modelling, Energy Convers. Manag. 196 (2019) 484–496. doi:10.1016/j.enconman.2019.05.099.

[15] H. Derbal-Mokrane, A. Benzaoui, A. M'Raoui, M. Belhamel, Feasibility study for hydrogen production using hybrid solar power in Algeria, Int. J. Hydrogen Energy. (2011). doi:10.1016/j.ijhydene.2010.06.078.

[16] M. Seitz, H. von Storch, A. Nechache, D. Bauer, Techno economic design of a solid oxide electrolysis system with solar thermal steam supply and thermal energy storage for the generation of renewable hydrogen, Int. J. Hydrogen Energy. (2017). doi:10.1016/j.ijhydene.2017.08.192.

[17] A. Mohammadi, M. Mehrpooya, Thermodynamic and economic analyses of hydrogen production system using high temperature solid oxide electrolyzer integrated with parabolic trough collector, J. Clean. Prod. (2019). doi:10.1016/j.jclepro.2018.11.261.

[18] J. Sanz-Bermejo, J. Muñoz-Antón, J. Gonzalez-Aguilar, M. Romero, Optimal integration of a solid-oxide electrolyser cell into a direct steam generation solar tower plant for zero-emission hydrogen production, Appl. Energy. 131 (2014) 238–247. doi:10.1016/j.apenergy.2014.06.028.

[19] J. Sanz-Bermejo, V. Gallardo-Natividad, J. González-Aguilar, M. Romero, Coupling of a solid-oxide cell unit and a linear fresnel reflector field for grid management, Energy Procedia. 57 (2014) 706–715. doi:10.1016/j.egypro.2014.10.226.

[20] M. Lin, S. Haussener, Techno-economic modeling and optimization of solar-driven high-temperature electrolysis systems, Sol. Energy. 155 (2017) 1389–1402. doi:10.1016/j.solener.2017.07.077.

[21] A. Mohammadi, M. Mehrpooya, Techno-economic analysis of hydrogen production by solid oxide electrolyzer coupled with dish collector, Energy Convers. Manag. 173 (2018) 167–178. doi:10.1016/j.enconman.2018.07.073.

[22] A. Ursua, L.M. Gandia, P. Sanchis, Hydrogen Production From Water Electrolysis: Current Status and Future Trends, Proc. IEEE. 100 (2012) 410–426. doi:10.1109/JPROC.2011.2156750.

[23] IRENA, Hydrogen from Renewable Power: Technology Outlook for the Energy Transition, 2018.

[24] S.H. Jensen, P.H. Larsen, M. Mogensen, Hydrogen and synthetic fuel production from renewable energy sources, Int. J. Hydrogen Energy. 32 (2007) 3253–3257. doi:10.1016/j.ijhydene.2007.04.042.

[25] H. Zhu, R.J. Kee, V.M. Janardhanan, O. Deutschmann, D.G. Goodwin, Modeling Elementary Heterogeneous Chemistry and Electrochemistry in Solid-Oxide Fuel Cells, J. Electrochem. Soc. 152 (2005) A2427. doi:10.1149/1.2116607.

[26] S. Campanari, P. Iora, Definition and sensitivity analysis of a finite volume SOFC model for a tubular cell geometry, J. Power Sources. 132 (2004) 113–126. doi:10.1016/j.jpowsour.2004.01.043.

[27] P. Iora, P. Aguiar, C.S. Adjiman, N.P. Brandon, Comparison of two IT DIR-SOFC models: Impact of variable thermodynamic, physical, and flow properties. Steady-state and dynamic analysis, Chem. Eng. Sci. 60 (2005) 2963–2975. doi:10.1016/j.ces.2005.01.007.

[28] NREL, NREL System Advisory Model, (n.d.). https://sam.nrel.gov/ (accessed April 14, 2019).

[29] L. Bernadet, G. Gousseau, A. Chatroux, J. Laurencin, F. Mauvy, M. Reytier, Influence of pressure on solid oxide electrolysis cells investigated by experimental and modeling approach, Int. J. Hydrogen Energy. 40 (2015) 12918–12928.

[30] G. Gavagnin, S. Rech, D. Sánchez, A. Lazzaretto, Optimum design and performance of a solar dish microturbine using tailored component characteristics, Appl. Energy. 231 (2018) 660–676. doi:10.1016/j.apenergy.2018.09.140.

[31] A. Giostri, Preliminary analysis of solarized micro gas turbine application to CSP parabolic dish plants, in: Energy Procedia, 2017. doi:10.1016/j.egypro.2017.12.124.

[32] I. Hischier, P. Leumann, A. Steinfeld, Experimental and numerical analyses of a pressurized air receiver for solar-driven gas turbines, in: ASME Int. Mech. Eng. Congr. Expo. Proc., 2010. doi:10.1115/IMECE2010-37843.

[33] Capstone, Product Catalog Capstone Microturbines. 2010, 2010.

[34] P. Fraser, P.S. a Klein, Stirling Dish System Performance Prediction Model, Mech. Eng. (2008).

[35] K. Lovegrove, A. Zawadski, J. Coventy, Paraboloidal Dish Solar Concentrators for Multi-Megawatt Power Generation, Proc. ISES. (2003).

[36] K. Lovegrove, W. Stein, Concentrating Solar Power Technology: Principles, Developments and Applications, 2012. doi:10.1533/9780857096173.

[37] T. Wendelin, Soltrace: A new optical modeling tool for concentrating solar optics, in: Int. Sol. Energy Conf., 2003. doi:10.1115/ISEC2003-44090.

[38] A. Giostri, E. Macchi, An advanced solution to boost sun-to-electricity efficiency of parabolic dish, Sol. Energy. (2016). doi:10.1016/j.solener.2016.10.001.

[39] K. Lovegrove, T. Taumoefolau, S. Paitoonsurikarn, P. Siangsukone, G. Burgess, A. Luzzi, G. Johnston, O. Becker, W. Joe, G. Major, Paraboiloidal dish solar concentrators for multi-Megawatt power generation, (2002).

[40] B.D. James, A.B. Spisak, W.G. Colella, Manufacturing cost analysis of stationary fuel

cell systems, Strateg. Anal. (2012) 1–143. https://www.sainc.com/assets/site_18/files/publications/sa 2015 manufacturing cost and installed price of stationary fuel cell systems_rev3.pdf.

[41] R. Rivera-Tinoco, C. Mansilla, C. Bouallou, Competitiveness of hydrogen production by High Temperature Electrolysis: Impact of the heat source and identification of key parameters to achieve low production costs, Energy Convers. Manag. (2010). doi:10.1016/j.enconman.2010.05.028.

[42] R. Anantharaman, O. Bolland, N. Booth, E. Van Dorst, C. Ekstrom, S. Fernandez, F. Franco, E. Macchi, G. Manzolini, D. Nikolic, A. Pfeffer, M. Prins, R. Sina, R. Laurence, European best practice guidelines for assessment of CO2 capture technologies, FP7 - ENERGY.2007.5.1.1 - Project no. 213206, 2011.

[43] S. Campanari, E. Macchi, Technical and Tariff Scenarios Effect on Microturbine Trigenerative Applications, in: Vol. 2 Turbo Expo 2003, ASME, 2003: pp. 747–757. doi:10.1115/GT2003-38275.

[44] U.S. Energy Information Administration, (2018). https://www.eia.gov/ (accessed February 7, 2019).

[45] M.R. Shaner, H.A. Atwater, N.S. Lewis, E.W. McFarland, A comparative technoeconomic analysis of renewable hydrogen production using solar energy, Energy Environ. Sci. (2016). doi:10.1039/c5ee02573g.

[46] H. Wang, W. Li, T. Liu, X. Liu, X. Hu, Thermodynamic analysis and optimization of photovoltaic/thermal hybrid hydrogen generation system based on complementary combination of photovoltaic cells and proton exchange membrane electrolyzer, Energy Convers. Manag. 183 (2019) 97–108. doi:10.1016/j.enconman.2018.12.106.

[47] A.C.W. Koh, L. Chen, W. Kee Leong, B.F.G. Johnson, T. Khimyak, J. Lin, Hydrogen or synthesis gas production via the partial oxidation of methane over supported nickel-cobalt catalysts, Int. J. Hydrogen Energy. 32 (2007) 725–730. doi:10.1016/j.ijhydene.2006.08.002.

[48] A.A. AlZahrani, I. Dincer, Design and analysis of a solar tower based integrated system using high temperature electrolyzer for hydrogen production, Int. J. Hydrogen Energy. (2016). doi:10.1016/j.ijhydene.2015.12.103.

[49] A. Mohammadi, M. Mehrpooya, A comprehensive review on coupling different types of electrolyzer to renewable energy sources, Energy. 158 (2018) 632–655. doi:10.1016/j.energy.2018.06.073.

[50] S. Koumi Ngoh, L.M. Ayina Ohandja, A. Kemajou, L. Monkam, Design and simulation of hybrid solar high-temperature hydrogen production system using both solar photovoltaic and thermal energy, Sustain. Energy Technol. Assessments. 7 (2014) 279–293. doi:10.1016/j.seta.2014.05.002.

[51] F. Sayedin, A. Maroufmashat, S. Sattari, A. Elkamel, M. Fowler, Optimization of Photovoltaic Electrolyzer Hybrid systems; Taking into account the effect of climate conditions, Energy Convers. Manag. (2016). doi:10.1016/j.enconman.2016.04.021.

[52] N.A. Kelly, T.L. Gibson, D.B. Ouwerkerk, A solar-powered, high-efficiency hydrogen fueling system using high-pressure electrolysis of water: Design and initial results, Int. J. Hydrogen Energy. (2008). doi:10.1016/j.ijhydene.2008.03.036.

[53] A. Abánades, C. Rubbia, D. Salmieri, Thermal cracking of methane into Hydrogen for a CO2-free utilization of natural gas, in: Int. J. Hydrogen Energy, 2013. doi:10.1016/j.ijhydene.2012.08.138.

[54] S. CONSONNI, F. VIGANO, Decarbonized hydrogen and electricity from natural gas, Int. J. Hydrogen Energy. 30 (2005) 701–718. doi:10.1016/j.ijhydene.2004.07.001.